



國立臺灣大學理學院物理所

碩士論文

Graduate Institute of Physics

College of Science

National Taiwan University

Master Thesis

高溫超導體/石墨烯約瑟芬元件製作與傳輸特性研究

Fabrication and transport properties in hybrid high-temperature  
superconductor/graphene Josephson junction

黃瀧毅

Lung-I Huang

指導教授：梁啟德 博士

王立民 博士

Advisors: Chi-Te Liang, Ph.D.

Li-Min Wang, Ph.D.

中華民國 103 年 7 月

July, 2014



國立臺灣大學碩士學位論文  
口試委員會審定書

高溫超導體/石墨烯約瑟芬元件製作與傳輸特性研究

Fabrication and transport properties in hybrid high-temperature  
superconductor/graphene Josephson junction

本論文係黃瀧毅君 (R00222045) 在國立臺灣大學物理學系物理  
所完成之碩士學位論文，於民國 102 年 6 月 21 日承下列考試委員審  
查通過及口試及格，特此證明

口試委員：

梁啟德

(簽名)

(指導教授)

梁啟德

林立弘

許民

## 誌謝



特別感謝梁啟德教授將我納入門下，教學風格具啟發性以及幽默風趣的個性打破我對指導教授的嚴厲刻板印象，教導我順利完成研究、論文、通過口試並取得碩士學位，且給我機會到美國國家標準技術研究院工作一年，這一切都衷心的感謝梁啟德老師，謝謝您的提攜。謝謝王立民教授的指導，從建構整個濺鍍系統到可以穩定的鍍出薄膜，以及實驗經驗、量測結果上的傳承，都使我受益良多。謝謝我在美國的老闆 Randolph Elmquist 博士，給我機會到 NIST 作研究，體驗美國人作研究的態度和方法。謝謝 Yanfei Yang 博士和 Yasuhiro Fukuyama 博士，是我在美國工作很好的實驗伙伴，從他們身上也學習到很多實驗的經驗和技巧。

謝謝林晃德博士，傳授給我許多觀念，包含課業、價值觀及人生許多的看法，碩士論文的校訂等...。謝謝胡德邦博士在物理觀念上的幫助以及碩士論文的提點；謝謝陳威仁博士在生活上對我們的照料以及實驗上的關心。謝謝智穎學長教導我使用黃光室的所有儀器，謝謝家翔、翊亭、舜聰學長實驗上的幫助，謝謝泛鴻、正全學長對於鍍超導膜的指導、謝謝承華學長在幫助我在元件上的製作，使得元件可以被製作完成並量測，謝謝智億學長微影蝕刻技巧的傳承，謝謝憲宏學長幫助我處理基板，謝謝蘇元鏘學長教導打線機的使用及量子干涉儀的量測。謝謝與我一起奮鬥的夥伴，裕峯、昌順同學，一起度過實驗上的難關，一起互相幫助，一起將所有課業、事務完成。謝謝台大物理碩士 100 級社團的各位好友，在整個碩士生活裡面有你們的作伴歡樂許多，很開心能夠在這一交到你們這群好友，祝你們前程似錦。

最後謝謝家人作為我強力的後援，讓我在讀碩士這條路上更加的有動力、信心，謝謝爸媽將我扶養長大，供我讀到碩士，一切的成果都獻給我的家人，謝謝你們。

## 摘要



本篇論文主題是高溫超導體與石墨烯約瑟芬界面 (Josephson Junction) 的製作與其電子傳輸特性的研究。想法來源為低溫超導體與石墨烯之間的安德烈夫反射現象 (Andreev reflection) 與鄰近效應 (proximity effect)，而我們則是選用高溫超導體 (EBCO) 與石墨烯製作出約瑟芬界面來試圖觀察上述的效應，並了解超導載子在界面中穿隧的物理機制，更希望能就藉由這個研究製作出更好的約瑟芬界面。

論文的另一個部分是研究外延石墨烯 (Epitaxial graphene) 的傳輸特性，我們觀察到絕緣態與量子霍爾態的相變與弱局部化 (Weak localization) 的效應。並且成功的將電子-電子散射 (electron-electron scattering)、電子-聲子散射 (electron-phonon scattering) 這兩種難以個別研究的散射機制藉由電子加熱效應 (current heating effect) 將其個別探討。

最後，我們的實驗成功製作出高溫超導與石墨烯的約瑟芬界面，而且觀察到在高溫超導體與石墨烯界面發生安德烈夫反射現象的證據。這是目前別人尚未做過的嘗試。期望在未來有更進一步的發展性，及前瞻性的應用。

# Abstract



In this thesis, the electron transport properties and the fabrication of Josephson junction in a hybrid high-temperature superconductor and graphene were investigated. The idea of adopting high-temperature superconductor, EuBaCuO (EBCO), and graphene derived from the Andreev reflection and proximity effect observed between the interface of the low-temperature superconductor and graphene; attempting to have a comprehensive picture of the aforementioned effects and the fundamental properties of the superconducting carriers in the Josephson junction in a variety of superconductors.

Besides what we mentioned in the previous paragraph, the rest of this thesis was dedicated to the study of the electrons transport properties in the epitaxial graphene. The behaviors of the insulator-quantum Hall transition and weak localization in the epitaxial graphene were observed in this study. Moreover, our experimental results suggested that the electron heating effect is a powerful tool for studying two scattering properties which are difficult to study independently and physical phenomena in two-dimensional systems or nanostructures.

Finally, we successfully demonstrated the fabrication of high-temperature superconducting/graphene Josephson junction and evidences responsible for Andreev reflection phenomenon observed in the high-temperature superconductors/graphene Josephson junction. The results of this unprecedented materials combination shed a light on the future development of its cutting-edge applications.

## Publication:



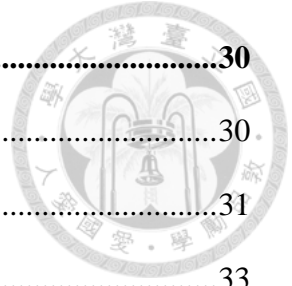
1. “Dirac fermion heating, current scaling, and direct insulator-quantum Hall transition in multilayer epitaxial graphene”, Fan-Hung Liu, Chang-Shun Hsu, Chiashain Chuang, Tak-Pong Woo, **Lung-I Huang**, Shun-Tsung Lo, Yasuhiro Fukuyama, Yanfei Yang, Randolph E Elmquist and Chi-Te Liang, *Nanoscale Research Letters* **8**, 360 (2013).
2. “Localization and electron-electron interactions in few-layer epitaxial graphene”, Shun-Tsung Lo, Fan-Hung Liu, Chang-Shun Hsu, Chiashain Chuang, **Lung-I Huang**, Yasuhiro Fukuyama, Yanfei Yang, Randolph E Elmquist and Chi-Te Liang, *Nanotechnology* **25**, 245201 (2014)
3. “Low Carrier Density Epitaxial Graphene Devices On SiC”, Yanfei Yang, **Lung-I Huang**, Yasuhiro Fukuyama, Fan-Hung Liu, Mariano A. Real, Paola Barbara, Chi-Te Liang, David B. Newell, Randolph E. Elmquist, to be published in *Small* (2014).

# Contents



|  |           |
|--|-----------|
| 誌謝 .....   | I         |
| 摘要 .....   | II        |
| Abstract.....  | III       |
| Contents .....   | IV        |
| List of figures.....   | VII       |
| <br>   |           |
| <b>Chapter 1 Introduction.....</b>                                   | <b>1</b>  |
| 1.1 Superconductors .....  | 1         |
| 1.1.1 Meissner effect.....   | 3         |
| 1.1.2 Type-I and Type-II superconductors .....                       | 4         |
| 1.2 Graphene .....   | 6         |
| <b>Chapter 2 Josephson effect.....</b>                               | <b>10</b> |
| 2.1 Macroscopic quantum model .....                                  | 10        |
| 2.2 Josephson equation.....  | 11        |
| 2.3 RCSJ model.....  | 14        |
| 2.4 Andreev reflection.....  | 16        |
| <b>Chapter 3 Experimental techniques and Sample fabrication.....</b> | <b>20</b> |
| 3.1 Fabrication of EBCO thin films .....                             | 20        |
| 3.2 Fabrication of SNS devices .....                                 | 21        |
| 3.3 Fabrication of SGS devices .....                                 | 24        |
| 3.4 Four-terminal resistance measurement.....                        | 25        |
| 3.5 Cryogenic system: Sorption pumping $^3\text{He}$ cryostat.....   | 27        |

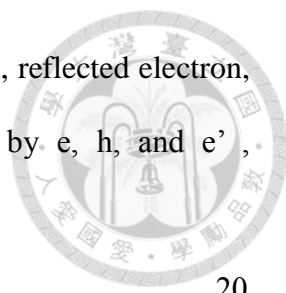
|  |           |
|--|-----------|
| <b>Chapter 4 Results of Epitaxial graphene .....</b>                   | <b>30</b> |
| 4.1 Characteristics of superconducting films .....                     | 30        |
| 4.1.1 Weak localization .....  | 31        |
| 4.2 Insulator-quantum Hall transition in epitaxial graphene .....      | 33        |
| 4.3 Weak localization and electron heating in epitaxial graphene ..... | 36        |
| <b>Chapter 5 Results of SGS .....</b>                                  | <b>49</b> |
| 5.1 Experimental results of EBCO thin films .....                      | 49        |
| 5.2 Experimental results of SNS .....                                  | 51        |
| 5.3 Experimental results of SGS .....                                  | 53        |
| <b>Chapter 6 Conclusion .....</b>                                      | <b>57</b> |



# List of figures



|   |    |
|---|----|
| Figure 1.1.1.....   | 2  |
| The development of the superconducting transition temperature with time.  |    |
| Figure 1.1.2.....   | 4  |
| Description of the perfect diamagnetism.  |    |
| Figure 1.1.3.....   | 5  |
| Magnetization $M$ and applied field $H$ for type-I and type-II Superconductors.   |    |
| Figure 1.2.1.....   | 6  |
| (a) Honeycomb lattice of a carbon monolayer. (b) Ambipolar electric field effect in single-layer graphene.  |    |
| Figure 2.2.1.....   | 11 |
| A schematic view of Josephson junction.   |    |
| Figure 2.2.2.....   | 12 |
| Different types of weak links: (a) SIS tunneling junction; (b) SNS tunneling junction.  |    |
| Figure 2.3.1.....   | 14 |
| Shows the $I$ - $V$ characteristic for a Josephson junction at $T = 0$ K. $I_c$ is the maximum supercurrent at zero voltage, and $I_n$ is the normal-state current. |    |
| Figure 2.3.2.....   | 15 |
| Shows a schematic representation of RCSJ model, $\otimes$ represents an ideal Josephson junction, $R$ is resistor, and $C$ is the capacitance.                      |    |
| Figure 2.4.1.....   | 16 |
| Shows a schematic of Andreev reflection in S/N interface.   |    |
| Figure 2.4.2.....   | 17 |
| Shows different scenarios of Andreev reflection in graphene: (a) $E_F \gg eV$ , retro-  |    |



reflection. (b)  $E_F = 0$ , specular reflection. (c) the incoming electron, reflected electron, and the Andreev reflected hole, called retro-reflection, denoted by  $e$ ,  $h$ , and  $e'$ , respectively; (d) shows the specular reflection.

Figure 3.1.1.....20

Shows a schematic of the RF sputtering system.

Figure 3.2.1.....22

Optical lithography technique for the SNS device. (a) Mask. (b) Patterned EBCO thin film on STO. (c) The SEM image for the superconductor bridge is the region that circled by dotted line in (a)(b).  $W$  is the width of bridge,  $W \sim 10 \mu m$ .

Figure 3.2.2.....22

(a) shows the schematic of the EBCO/Au/EBCO structure, (b) is the SEM diagram of the EBCO bridge cut by focus ion beam (FIB), and (c) is the SEM image of the squared region in (b), where  $W$ ,  $\sim 10 \mu m$ , is the width of bridge, and  $L$ ,  $\sim 107 nm$ , is the length of the gap.

Figure 3.3.1.....24

Shows a schematic representation of different structures of SGS devices; (a) structure previously used for metallic superconductors, and (b) a novel device structure for high-temperature superconductors, where SC is the abbreviation of superconductor.

Figure 3.4.1.....25

The electrical configuration for van der Pauw method with an arbitrary shape and four contacts located at the peripheral. The resistance  $R_{MN,OP}$  is a voltage difference between contact M and N, current source is passing through contacts O and P.

Figure 3.4.2.....27

The configuration of four-terminal measurement.



Figure 3.5.1.....28

Shows a schematic diagram of Oxford instrument.

Figure 3.5.2.....28

The process of  $^3\text{He}$  condensation. It shows releasing of  $^3\text{He}$  gas.

Figure 4.1.1.....30

(a) the unit cell structure of SiC, (b) a kind of SiC polytypes, 6H. “6” refers to a stack of periodically arranged number (ABCACB), the letter “H” denotes the hexagonal symmetry of the SiC crystal. A and B only difference between shift of the lattice, their orientation do not change. But C means twisting the lattice by  $60^\circ$ .

Figure 4.1.2.....32

A schematic shows the time reversal trajectory of electrons between A and B, where O is the origin, C and C' denote the amplitudes of the wave functions of electrons moving clockwise and counter-clockwise, respective.

Figure 4.2.1.....33

The curves of  $\rho_{xx}$  at different temperatures in high-field I-QH transition.

Figure 4.2.2.....34

The diagram of  $\ln |\text{d}\rho_{xx} / \text{d}B| B_c$  vs  $\ln T$ . From the slope, we obtain the scaling exponent  $\kappa \approx 0.26$ .

Figure 4.3.1.....37

Depicts the results of weak localization observed in an epitaxial graphene in the low magnetic field at different temperatures.

Figure 4.3.2.....37

Shows the resistivity  $\rho_{xx}$  as a function of temperature.

Figure 4.3.3.....38

Weak localization of epitaxial graphene in the low magnetic field with different currents.

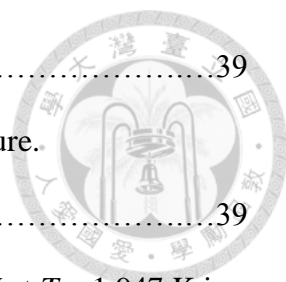


Figure 4.3.4.....39

Shows resistivity  $\rho_{xx}$  linear dependence on the increasing temperature.

Figure 4.3.5.....39

Shows the electron effective temperature  $T_e$  as a function of current  $I$  at  $T = 1.947$  K in a logarithmic scale. The linear line represents a power law  $T_e \propto I^\alpha$  with the exponent  $\alpha = 0.54$ . When the current is below  $10 \mu\text{A}$ , we cannot observe the dependence between  $T_e$  and  $I$ ; on the contrary, we observe the linear dependence at high current ( $I > 20 \mu\text{A}$ ).

Figure 4.3.6.....41

Shows the results of the weak localization in the low magnetic field at different temperatures. Curves are shifted such that the peak of WL peak is at  $0 \Omega$ . We can clearly observe the decreasing peak height of WL with the increasing temperature.

Figure 4.3.7.....42

Shows a diagram  $\Delta\rho_{xx}(B) = \rho_{xx}(B) - \rho_{xx}(B = 0)$  (in black curve) vs. magnetic field  $B$ , the red curve is a fitting curve by eq. (4.3.3), at  $T = 3\text{K}$ .

Figure 4.3.8.....43

(a) The lattice temperature dependence of the coherence length. (b) The current dependence of the coherence length.

Figure 4.3.9.....44

(a) The lattice temperature ( $T_L$ ) shows a linear dependence on the phase coherence rate ( $1/\tau_\phi$ ). (b) It shows current dependence of the phase coherence rate at a fixed temperature  $T_L = 1.95\text{K}$ .

Figure 4.3.10.....46

Shows the electron effective temperature  $T_e$  as a function of current  $I$  at  $T = 1.947\text{K}$ . The linear line represents a power law  $T_e \propto I^\alpha$  with the exponent  $\alpha = 0.48$ .

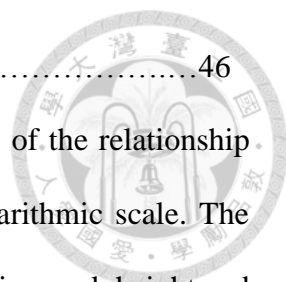


Figure 4.3.11.....46  
Illustrates the comparison of the results from two different analyses of the relationship between the injected current and the electron temperature in a logarithmic scale. The slopes of the straight lines obtained by the analyses of weak localization peak height and phase coherent rate are 0.54 and 0.48, respectively.

Figure 5.1.1.....49  
Shows the XRD diagrams of the EBCO thin film.

Figure 5.1.2.....50  
Shows the  $R$ - $T$  diagrams of the EBCO thin films, at different temperature and sputtering gas pressure.

Figure 5.2.1.....51  
(a) is the SEM diagram of the EBCO bridge cut by focus ion beam (FIB), where  $W$ ,  $\sim 10 \mu\text{m}$ , is the width of the bridge, and (b) is the enlarged SEM image of the squared region in (a). The gap is about 120nm.

Figure 5.2.2.....52  
The  $R$ - $T$  diagram of the SNS sample.

Figure 5.3.1.....53  
Shows the  $R$ - $T$  diagram of the EBCO electrodes.

Figure 5.3.2.....54  
Shows the  $I$ - $V$  curve of the EBCO electrodes at  $T = 11 \text{ K}$ . The critical current can be seen at around  $I = 50 \text{ mA}$ .

Figure 5.3.3.....54  
Shows the  $I$ - $V$  curve of the SGS junction at  $T = 11 \text{ K}$ .

# Chapter 1 Introduction



In this thesis, we focused on the hybrid EuBaCuO (EBCO) and graphene device, EBCO/graphene/EBCO Josephson junction. “Josephson” effect was considered by Phil Anderson before 1962 [1], but he did not give a reasonable explanation for the phenomenon; considering the junction was too short or the destruction of the insulating wall responsible for the conduction between the superconductors. Brian David Josephson gave the phenomenon an explanation [2] by claiming that it was due to the tunneling of Cooper pairs through the weak link sandwiched by two superconductors; called Josephson effect. In order to understand the physics of our device, made of EBCO/graphene/EBCO, we need to know first the basic characteristics of superconductors and graphene. The following sections will be dedicated to that followed by mathematical explanations about the Josephson effect in the next chapter.

## 1.1 Superconductors

Heike Kamerlingh Onnes and his colleagues found a special phenomenon by cooling mercury down to the boiling temperature of liquid helium (4.2 K) in 1911. They are the first group observing the superconductivity while the electrical resistance of mercury suddenly dropped to zero [3]. Since then, researchers started investigating superconductivity of different materials, especially those with higher critical temperature ( $T_c$ ), defined by the temperature with zero resistance. The zero resistance is known as an important phenomenon of the superconductor. When the temperature of a superconductor

decreases to the  $T_c$ , a transition from normal state to the superconducting one happens. Figure 1.1.1 shows the development of superconductors, as well as the corresponding  $T_c$ , with time; from  $T_c = 7$  K for lead in 1913 and 15 K for niobium in 1950 [4] to  $T_c > 150$  K in 2013 [5]. A more aggressive purpose is that people are looking for a room-temperature superconductor.

In this study, we choose EBCO to fabricate our device. It is very similar to the famous high  $T_c$  superconductor, YBCO, and easy to grow at a critical temperature higher than the boiling point of liquid nitrogen (77 K).

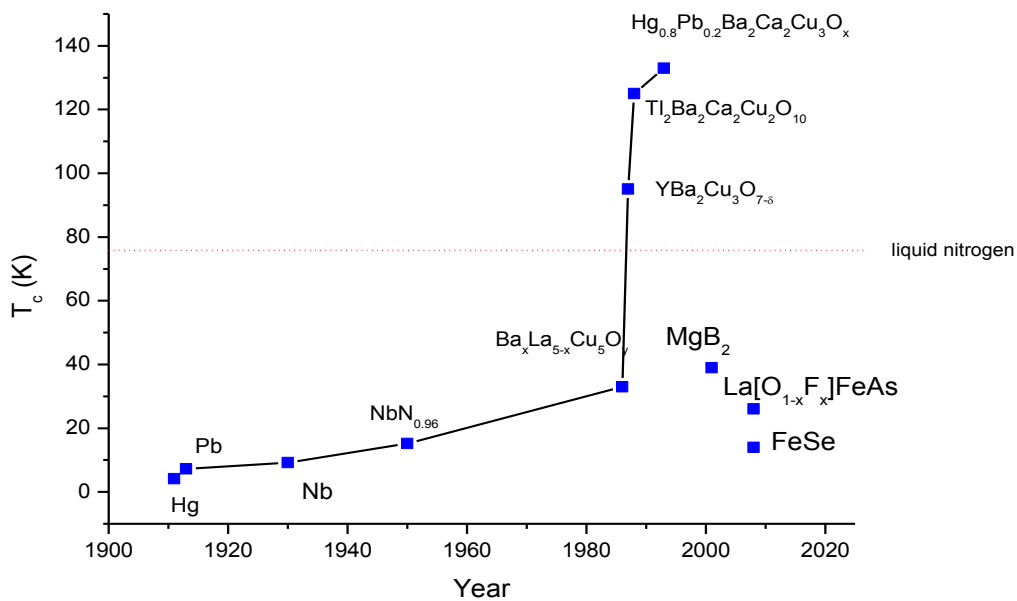
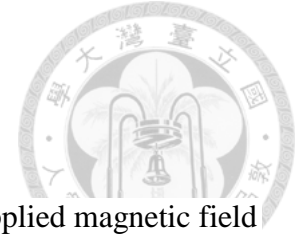


Figure 1.1.1: The development of the superconducting transition temperature with time [4].

### 1.1.1 Meissner effect



When a superconductor is at the temperature above its  $T_c$ , an applied magnetic field can pass through its interior, i.e., a magnetic field is present inside the superconductor. However, when the temperature is below  $T_c$ , the magnetic field applied inside the superconductor will be expelled from within. That is called the diamagnetic (Diamagnetism); a phenomenon used for the application of magnetic suspension. This phenomenon was discovered by Meissner in 1933; known as the Meissner effect. The application of the external magnetic field before or after the superconductor reaching its  $T_c$  will result in the same phenomenon; no magnetic field existed inside the superconductor [8]. It can also be explained by the electromagnetism. The relation among magnetic induction  $\vec{B}$ , magnetic field  $\vec{H}$ , and total magnetization  $\vec{M}$  can be expressed as:

$$\mathbf{B} = \mu_0(\mathbf{M} + \mathbf{H}), \quad (1.1.1)$$

where  $\mu_0$  is the permeability of free space, and  $\chi = \frac{M}{H}$  is the magnetic susceptibility.

Susceptibility  $\chi = -1$  represents a perfect diamagnetism in a superconductor when the temperature of superconducting material is below its critical temperature. In other words, the  $B$  field cannot exist inside a superconductor. When we applied a magnetic field on a superconductor, it will generate an opposite magnetization  $M$  to oppose against the applied field  $H$ .

$$\mathbf{M} = -\mathbf{H}. \quad (1.1.2)$$

Two basic phenomena shown above can be observed in each superconductor and explained by an important theory, Bardeen-Cooper-Schrieffer (BCS) theory [6]. However, the BCS theory cannot explain all the phenomena observed in the high- $T_c$  superconductor

(HTS) very well.

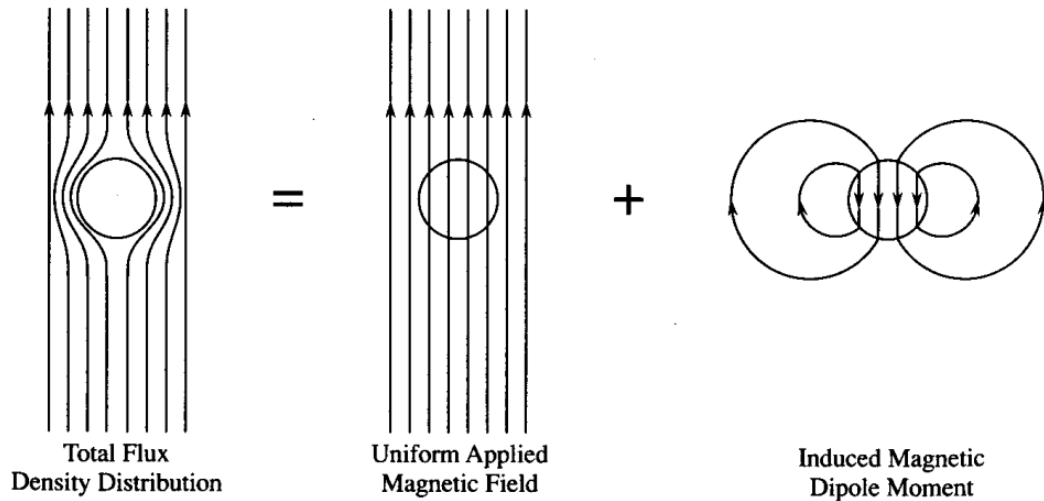
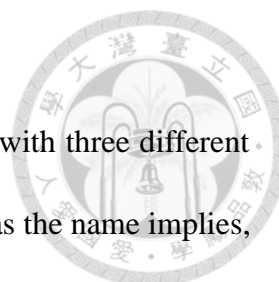


Figure 1.1.2: Description of the perfect diamagnetism. [7]

### 1.1.2 Type-I and Type-II superconductors

From the last section we learned that a magnetic flux will be excluded from inside of the superconductor due to the Meissner effect. But the Meissner effect can be destroyed when a strong enough magnetic field is applied to the superconductor. That critical magnetic field,  $H_c$ , can be used to explain different behaviors of type I and type II superconductors shown in figure 1.1.3.

Usually for type I superconductors, the superconductivity will totally disappear when the applied magnetic field is above a critical value  $H_c$ ; namely type I superconductor is back to the normal state with zero magnetization  $\mathbf{M}$ . Pure metals, such as lead, aluminum, and mercury [7], typically exhibit type I superconductivity.



In case of Type II superconductors, they are normally alloys with three different states, superconducting, normal, and mixed states. The mixed state, as the name implies, means that the superconducting and normal states coexist at the same time. So there are two different critical fields,  $H_{c1}$  and  $H_{c2}$ , in the type-II superconductor. All of the high-temperature superconductors belong to type-II; EBCO is no exception.

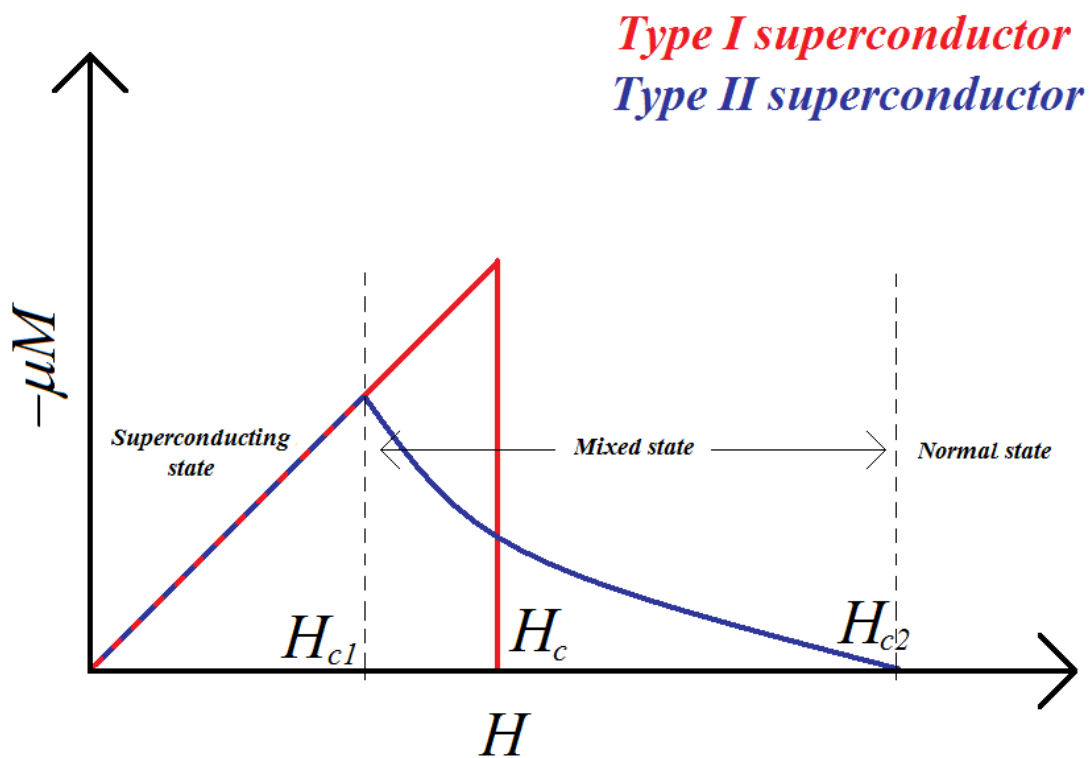


Figure 1.1.3: Magnetization  $M$  and applied field  $H$  for type-I and type-II Superconductors [9].



## 1.2 Graphene

Graphene is a single atomic layer of graphite. The structure of graphene contains a honeycomb lattice of carbon atoms in a perfect two-dimensional (2D) layer. It was not known to exist in an isolated form until 2004. The electron transport properties were reported from some research groups [10-12].

Due to the unusual properties of graphene, such as quasiparticle, massless Dirac fermion and the relativistic-like behaviors [11, 12], ambipolar field effect [10], “half-integer” quantum Hall effect [11], high crystal quality, and ballistic transport at submicron distances [10, 11]. More explorations of graphene have been conducted since its discovery for the years to come.

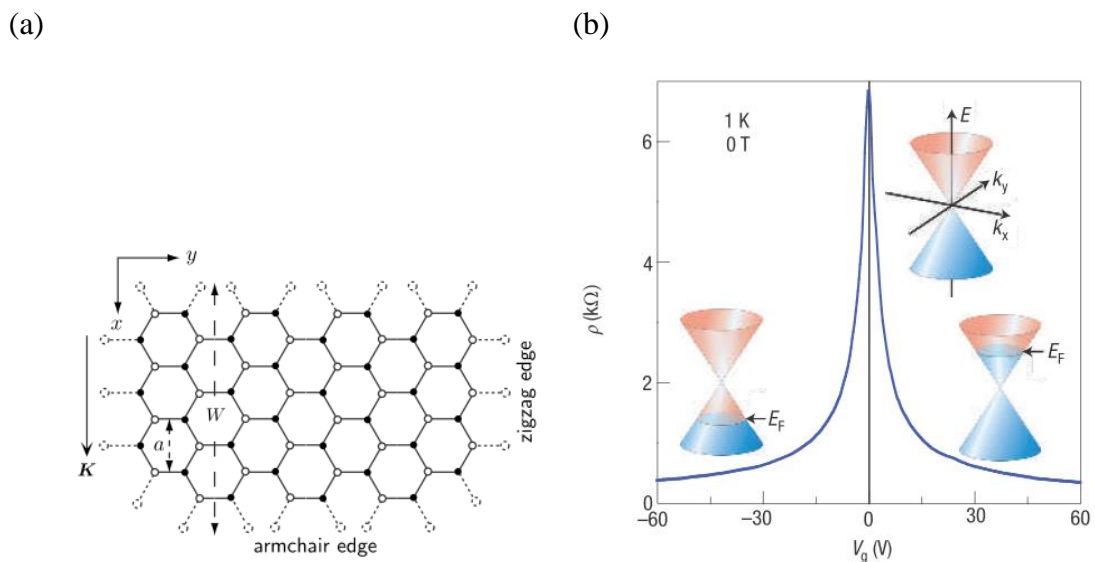
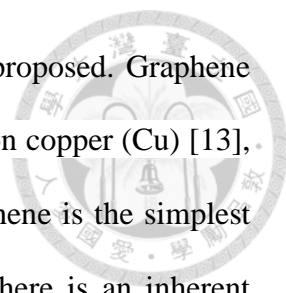


Figure 1.2.1: (a) Honeycomb lattice of a carbon monolayer [15]. (b) Ambipolar electric field effect in single-layer graphene. [16]



Recently, several methods of producing graphene films were proposed. Graphene can be fabricated by exfoliation, chemical vapor deposition (CVD) on copper (Cu) [13], or epitaxially grown on Silicon carbide (SiC) [14]. Exfoliated graphene is the simplest one; formed by mechanically using tape cleavage. Nevertheless, there is an inherent problem in this technique: the size of graphene can be only in microns. It is not a scalable technique and really hard to locate the graphene film. CVD graphene and epitaxial graphene can be used to produce large area pieces. Moreover, epitaxy produces higher quality and uniform films than CVD, which is not detailed in this study. The epitaxial graphene was formed on the Si face of a high-purity SiC wafer by thermal annealing and that is the main source of graphene in this thesis. We will show more measurements results regarding to epitaxial graphene [17, 18] in the later chapters.

## References



- [1] B. D. Josephson, *Proceedings of the IEEE* **62**, 6, 838 - 841, (1974).
- [2] B. D. Josephson, *Phys. Lett* **1**, 7, 251-253 (1962).
- [3] H. K. Onnes, *Commun. Phys. Lab. Univ. Leiden* **12**, 120, (1911).
- [4] Charles P. Poole, Jr., Horacio A. Farach, Richard J. Creswick, “*Superconductivity*”, (Academic Press, 1995).
- [5] Nao Takeshita, Ayako Yamamoto, Akira Iyo, and Hiroshi Eisaki, *J. Phys. Soc. Jpn.* **82**, 023711 (2013).
- [6] J. Bardeen, L. N. Cooper, and J. R. Schrieffer, *Physical Review* **108**, 1175 (1957).
- [7] Webpage” Lecture 8: Perfect Diamagnetism”, Terry P. Orlando, Massachusetts Institute of Technology, 2003, Retrieved April 11, (2012).  
<http://web.mit.edu/6.763/www/FT03/Lectures/Lecture8.pdf>
- [8] Allister M Forrest, *Eur J. Phys.* **4**, 17 (1983).
- [9] Webpage” Fichier: Magnetisation\_and\_superconductors.png”, Retrieved April 11, (2012).  
[http://fr.wikipedia.org/wiki/Fichier:Magnetisation\\_and\\_superconductors.png](http://fr.wikipedia.org/wiki/Fichier:Magnetisation_and_superconductors.png)
- [10] K. S. Novoselov, A. K. Geim, S. V. Morozov, D. Jiang, Y. Zhang, S. V. Dubonos, I. V. Grigorieva, and A. A. Firsov, *Science* **306**, 666 (2004).
- [11] K. S. Novoselov, A. K. Geim, S. V. Morozov, D. Jiang, M. I. Katsnelson, I. V. Grigorieva, S. V. Dubonos, and A. A. Firsov, *Nature* **438**, 197 (2005).
- [12] Y. Zhang, Y.-W. Tan, H. L. Stormer, and P. Kim, *Nature* **438**, 201 (2005).
- [13] X. Li, W. Cai, J. An, S. Kim, J. Nah, D. Yang, R. Piner, A. Velamakanni, I. Jung, E. Tutuc, S. K. Banerjee, L. Colombo, and R. S. Ruoff, *Science* **324**, 1312 (2009).
- [14] Johannes Jobst, Daniel Waldmann, Florian Speck, Roland Hirner, Duncan K.

- Maude, Thomas Seyller, and Heiko B. Weber<sup>1</sup>, *Phys. Rev. B* **81**, 195434 (2010).
- [15] C. W. J. Beenakker, *Rev. Mod. Phys.* **80**, 1337-1354 (2008).
- [16] A. K. Geim, K. S. Novoselov, *Nature Materials* **6**, 183 (2007).
- [17] Gregory M. Rutter, Nathan P. Guisinger, Jason N. Crain, Phillip N. First, and Joseph A. Stroscio, *Phys. Rev. B* **81**, 245408 (2010).
- [18] Y.-M. Lin, C. Dimitrakopoulos, K. A. Jenkins, D. B. Farmer, H.-Y. Chiu, A. Grill, Ph. Avouris, *Science* **327**, 5966 (2010).



## Chapter 2 Josephson effect



The Josephson effect is the phenomenon of a supercurrent; a current that flows through a junction without any applied voltage. Devices known as the Josephson junction consist of two superconductors sandwiching a weak link, which can be an insulating layer (superconductor / insulator / superconductor junction, or S-I-S), a non-superconducting metal (S-N-S), or a thin layer of graphene (S-G-S). From another perspective, the Josephson effect can be viewed as an example of a macroscopic quantum phenomenon, which will be explained in the following section.

### 2.1 Macroscopic quantum model

When a superconductor is at the temperature below its critical temperature, two electrons with opposite momentums and spin directions near the Fermi surface can be combined into Cooper pairs, which are composite bosons [5]. It is not affected by the limit of the Pauli exclusion principle which allows different bosons in the same quantum state. Large number of Cooper pairs will condense into the same quantum state, the ground state. A macroscopic phenomenon, Josephson effect, can be observed when most of the bosons with the same behavior stay in the same state. Therefore, the behavior of Josephson junction related to the Cooper pairs can be described by using a single wave function. A macroscopic quantum model followed can be utilized to explain this quantum phenomenon. Josephson tunneling junction formed by combining two superconductors exhibits a barrier to the electrons. A certain phase difference, attributed to the tunneling effect and phase interference, between the macroscopic wave functions of the device, cause the Josephson effect.

## 2.2 Josephson equation

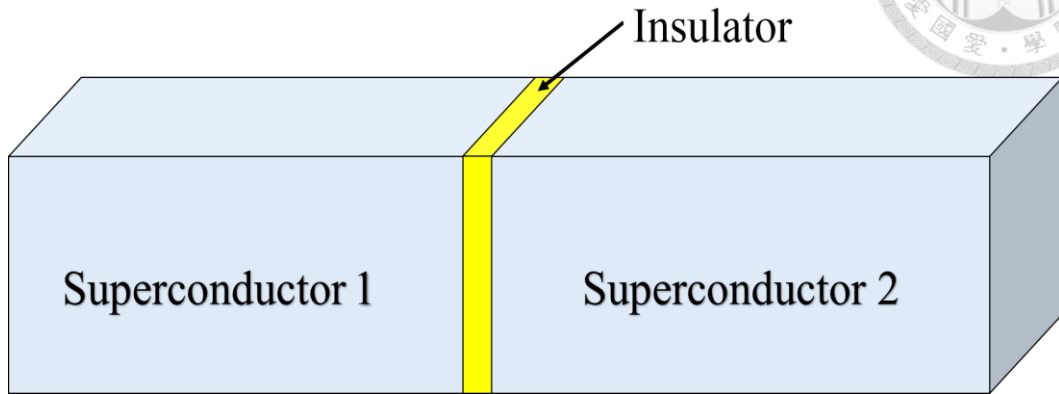


Figure 2.2.1: A schematic view of Josephson junction.

A schematic description of a Josephson junction obtained by inserting an insulating layer between two superconductors is shown in figure 2.2.1. When the insulating layer is very thin, some degree of weak coupling between two superconductors exists. A phase correlation, due to the weak coupling, between superconductors makes Cooper pairs penetrating this barrier from superconductor 1 into superconductor 2. In order to realize the tunneling of the Cooper pairs in a Superconductor/Insulator/Superconductor (SIS) device, the thickness of the insulating layer needs to be within approximately  $10 \text{ \AA}$  due to the slim probability of tunneling in the SIS structure. Figure 2.2.2 (a) and (b) illustrate two possible schemes to observe the tunneling phenomenon. Figure 2.2.2 (b) shows another structure called a Superconductor/Non-superconducting metal/Superconductor (SNS) device. As long as the thickness of the non-superconducting metal is kept below about 100 nm, there is the opportunity to observe the tunneling effect of the Cooper pairs.

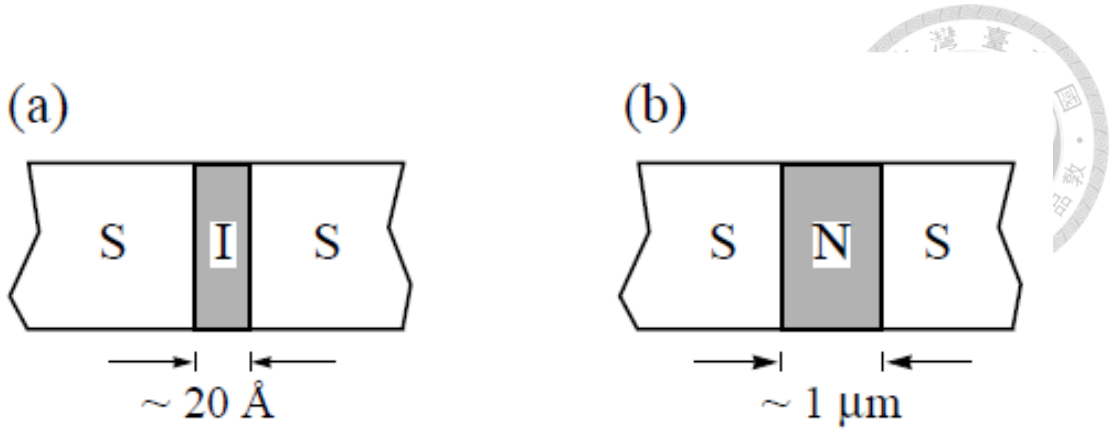


Figure 2.2.2: Different types of weak links: (a) SIS tunneling junction; (b) SNS tunneling junction. [1]

For a mathematical explanation, let us consider two superconductors, denoted as 1 and 2, respectively, separated by an insulating barrier (SIS structure). From a macroscopic quantum model, the time-dependent Schrödinger equation for the superconductor can be given by:

$$i\hbar \frac{\partial \psi}{\partial t} = H\psi, \quad (2.2.1)$$

where  $\psi$  and  $H$  are the wave functions and Hamiltonians for superconductors, respectively.

So we can write down the wave functions of the electrons in the superconductors with the weak coupling as follows:

$$i\hbar \frac{\partial \psi_1}{\partial t} = E\psi_1 + K\psi_2, \quad (2.2.2)$$

$$i\hbar \frac{\partial \psi_2}{\partial t} = E\psi_2 + K\psi_1, \quad (2.2.3)$$

where  $K$  is the coupling constant, deciding the tunneling probability of Cooper pairs. Due to the weak coupling existing between the superconductors, the constant  $K$  is very small.

Then we express the wave functions in terms of the pair density as the following:

$$\psi_1 = \sqrt{\rho_1} e^{i\theta_1} \quad \text{and} \quad (2.2.4)$$

$$\psi_2 = \sqrt{\rho_2} e^{i\theta_2}, \quad (2.2.5)$$

where  $\rho_1$  and  $\rho_2$  are the densities of super electrons in superconductors.

If the wave functions in equations (2.2.4) and (2.2.5) are substituted into equations (2.2.2) and (2.2.3), we can separate the real and the imaginary parts and obtain equations as the following:

$$\frac{\partial \rho_1}{\partial t} = \frac{2K}{\hbar} \sqrt{\rho_1 \rho_2} \sin(\theta_2 - \theta_1) \quad (2.2.6)$$

$$\frac{\partial \theta_1}{\partial t} = -\frac{E_1}{\hbar} - \frac{K}{\hbar} \sqrt{\frac{\rho_1}{\rho_2}} \cos(\theta_2 - \theta_1) \quad (2.2.7)$$

$$\frac{\partial \rho_2}{\partial t} = -\frac{2K}{\hbar} \sqrt{\rho_1 \rho_2} \sin(\theta_2 - \theta_1) \quad (2.2.8)$$

$$\frac{\partial \theta_2}{\partial t} = -\frac{E_2}{\hbar} - \frac{K}{\hbar} \sqrt{\frac{\rho_1}{\rho_2}} \cos(\theta_2 - \theta_1) \quad (2.2.9)$$

If both of the superconductors are the same material, which means  $\rho_1 = \rho_2 = \rho$ , we can have the relation between equations (2.2.6) and (2.2.8) as the following:

$$\frac{\partial \rho_1}{\partial t} = -\frac{\partial \rho_2}{\partial t}. \quad (2.2.10)$$

The equation shows the increasing rate of the Cooper pairs density in superconductor 1 is equal to the decreasing rate of the Cooper pairs density in superconductor 2. The current density of the Cooper pairs can be shown as the following:

$$\begin{aligned} j_s &= 2e \frac{\partial \rho_1}{\partial t} = \frac{2eK}{\hbar} \rho \sin \phi \\ j_s &= j_c \sin \phi, \end{aligned} \quad (2.2.11)$$

where  $j_c = \frac{2eK\rho}{\hbar}$  is the critical current density,  $\phi$  is the phase difference, and  $K$  is the coupling constant. Then we subtract eq. (2.2.7) from eq. (2.2.9) and obtain:

$$\frac{\partial(\theta_2 - \theta_1)}{\partial t} = \frac{\partial \phi}{\partial t} = \frac{1}{\hbar} (E_1 - E_2). \quad (2.2.12)$$

If the potential difference between the superconductors is  $V$ , the energy difference for an electron traveling through them is  $2 eV$ ; therefore,

$$\frac{\partial \phi}{\partial t} = \frac{2eV}{\hbar} . \quad (2.2.13)$$

Eqs. (2.2.11) and (2.2.13) are called “Josephson relations”, and that describe the basic tunneling behavior of Cooper pairs across the junction.

### 2.3 RCSJ model

The resistively and capacitively shunted junction (RCSJ) model is an easy and useful equivalent-circuit model to quantify the behavior of a Josephson junction. It is composed of a resistor and a capacitor, parallelly connected to an ideal Josephson junction with a critical current. A supercurrent exists when we apply a constant current  $I < I_c$  because there is zero resistance in the junction. On the contrary, if we apply a constant current  $I > I_c$  flowing through the Josephson junction, a normal current  $I_n$  must start flowing because the supercurrent cannot exceed  $I_c$ . That can be seen more clearly in figure 2.3.1.

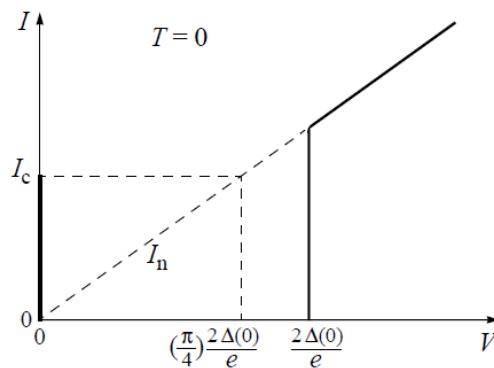


Figure 2.3.1: Shows the  $I$ - $V$  characteristic for a Josephson junction at  $T = 0$  K.  $I_c$  is the maximum supercurrent at zero voltage, and  $I_n$  is the normal-state current [1].

Then, we can simplify RCSJ model illustrated in figure 2.3.2. By the mathematical derivation followed, more details of this model will be revealed. When the current flowing through the Josephson junction is  $I > I_c$ , the voltage  $V$  across the junction is not zero while the superconductors are still in the superconducting state. Not only the Josephson current but also the normal current flows through the junction. The time-dependent current passing through the junction in terms of capacitance can be represented as follows:

$$I = I_d + I_n + I_s = C \frac{dV(t)}{dt} + \frac{V(t)}{R} + I_c \sin \phi, \quad (2.3.1)$$

where  $I_s$ ,  $I_n$ , and  $I_d$  are the super, normal, and displacement currents, respectively. ( $I_d = C \frac{dV(t)}{dt}$ )

From the AC Josephson equation:

$$\frac{d\phi}{dt} = \frac{2eV(t)}{\hbar} \quad (2.3.2)$$

, eqn. 2.3.1 can be written as:

$$I = \frac{\hbar C}{2e} \frac{d^2\phi(t)}{dt^2} + \frac{\hbar}{2eR} \frac{d\phi(t)}{dt} + I_c \sin \phi. \quad (2.3.3)$$

In fact, Josephson junction in an electric circuit can be substituted by the following equivalent circuit shown in figure 2.3.2. The equivalent circuit model is called resistively and capacitively shunted junction; abbreviated as RCSJ model.

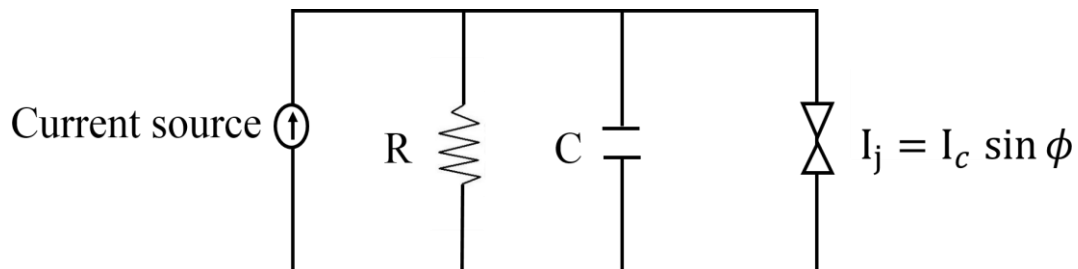


Figure 2.3.2: Shows a schematic representation of RCSJ model, represents an ideal Josephson junction, R is resistor, and C is the capacitance.

## 2.4 Andreev reflection



In this thesis, we study the Josephson effect in a high-temperature/graphene hybrid junction. Andreev reflection in our devices happened when the temperature of device is below  $T_c$ , at which electrodes were in the superconducting state leaving the graphene in the normal state; therefore, a superconducting state/normal state (S/N) interface formed. The Andreev reflection occurs at the S/N interface. A hole in the N region will be reflected when an incoming electron from the N region hits the S/N interface as shown in figure 2.4.1. Therefore an electron pair (Cooper pair) will transport in S region. In other words, if the electron in the conduction band is in the excited state below the superconducting gap, two possible ways occur. The electron can be either normally reflected at S/N interface or paired with another electron possessing opposite momentum and spin to form a Cooper pair tunneling through the S/N interface. Each Andreev reflection transfers a charge of  $2e$  across the interface and causes a retroreflection (AR) [3] of a hole of opposite spin and momentum to the incident electron.

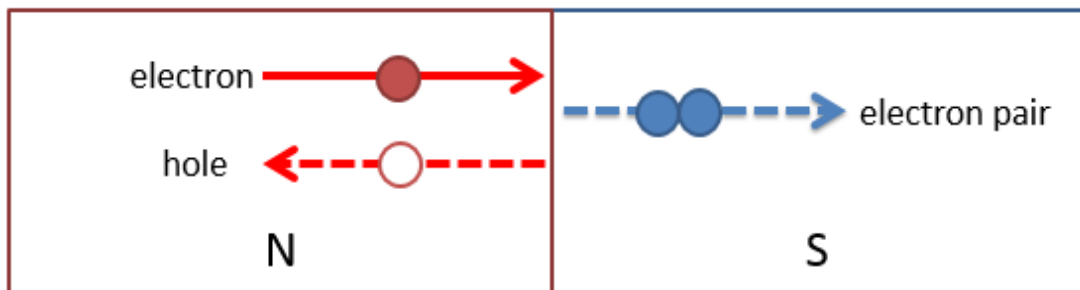


Figure 2.4.1: Shows a schematic of Andreev reflection in S/N interface.

But difference between using the normal metal or graphene as the sandwiched layer exists. The Andreev reflection of a normal metal behaves the same as mentioned above in figure 2.4.1. If graphene is used to replace the metal between the superconductors, retroreflection (AR) and specular Andreev reflection (SAR), which will be present in the superconductor/graphene/superconductor devices [2], can be observed.

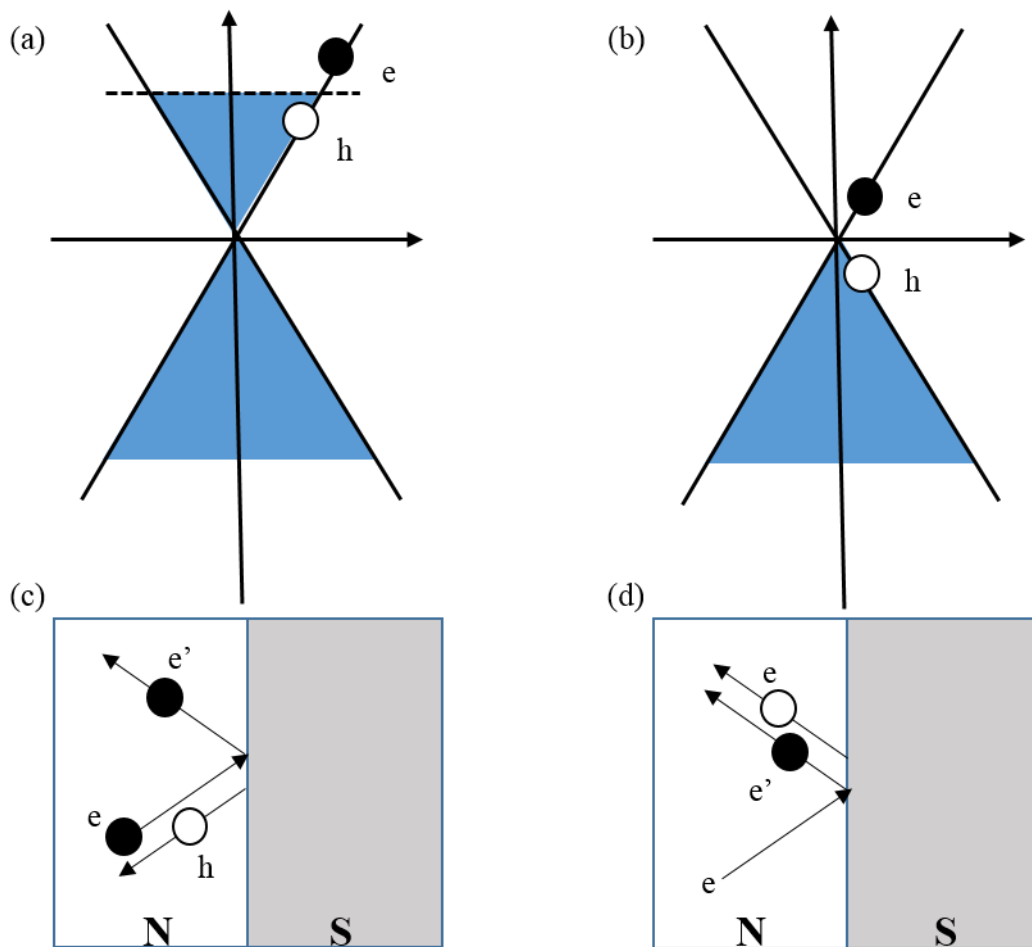
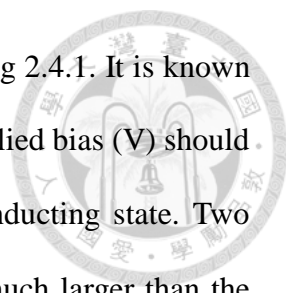


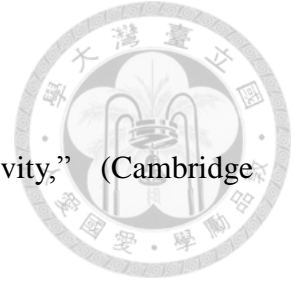
Figure 2.4.2: Shows different scenarios of Andreev reflection in graphene: (a)  $E_F \gg eV$ , retro-reflection. (b)  $E_F = 0$ , specular reflection. (c) the incoming electron, reflected electron, and the Andreev reflected hole, called retro-reflection, denoted by  $e$ ,  $h$ , and  $e'$ , respectively; (d) shows the specular reflection [4].



The basic idea of Andreev reflection in graphene is shown in Fig 2.4.1. It is known that any Cooper pair will exist only at a finite bias; therefore, the applied bias ( $V$ ) should not exceed the superconducting gap in order to keep the superconducting state. Two conditions can be considered. Firstly, when Fermi energy ( $E_F$ ) is much larger than the superconducting gap and the bias of junction is smaller than the superconducting gap ( $V < \Delta \ll E_F$ ) as shown in figure 2.4.2 (a) and (c), referring to the retro-reflection (AR). Secondly, if the Fermi energy is smaller than the superconducting gap, normally at  $E_F = 0$  possibly achieved by tuning the gate, fabricated by graphene, to adjust the junction bias below the superconducting gap and the electron energy above Fermi energy ( $0 = E_F < eV < \Delta$ ), corresponding to the specular reflection (SAR) as shown in Fig 2.4.1 (b) and (d).

In order to understand how the hybrid HTS/graphene device, structured by EBCO/graphene/EBCO works, the aforementioned fundamental properties of superconductors and graphene are necessary to investigate and analyze the results of the devices in this study.

## References



- [1] Andrei Marouchkine, “Room-Temperature Superconductivity,” (Cambridge International Science Publishing, (2004).
- [2] Katsuyoshi Komatsu, Chuan Li, S. Autier-Laurent, H. Bouchiat, and S. Gueron, *Phys. Rev. B* **86**, 115412 (2012)
- [3] Pablo Buset Atienza, *Superconducting proximity effect and nonlocal transport in graphene and carbon nanotubes* (April 2012).
- [4] Xing Lan Liu, *Quantum Dots and Andreev Reflections in Graphene* (August 2010).
- [5] M. de Llano, F. J. Sevilla and S. Tapia, *Int. J. Mod. Phys. B* **20**, 2931 (2006).

# Chapter 3 Experimental technique and Sample fabrication



In this thesis, two novel materials were fabricated to form the EBCO/graphene/EBCO structure. The configuration of the RF sputtering system, used to grow EBCO thin film, will be introduced first; followed by the fabrication of graphene on the EBCO bridge and then the measurement.

## 3.1 Fabrication of EBCO thin films

In order to produce EBCO/graphene/EBCO devices, we need to grow EBCO thin film on SrTiO<sub>3</sub> (STO) substrate. The RF sputtering system used is shown in figure 3.1.1.

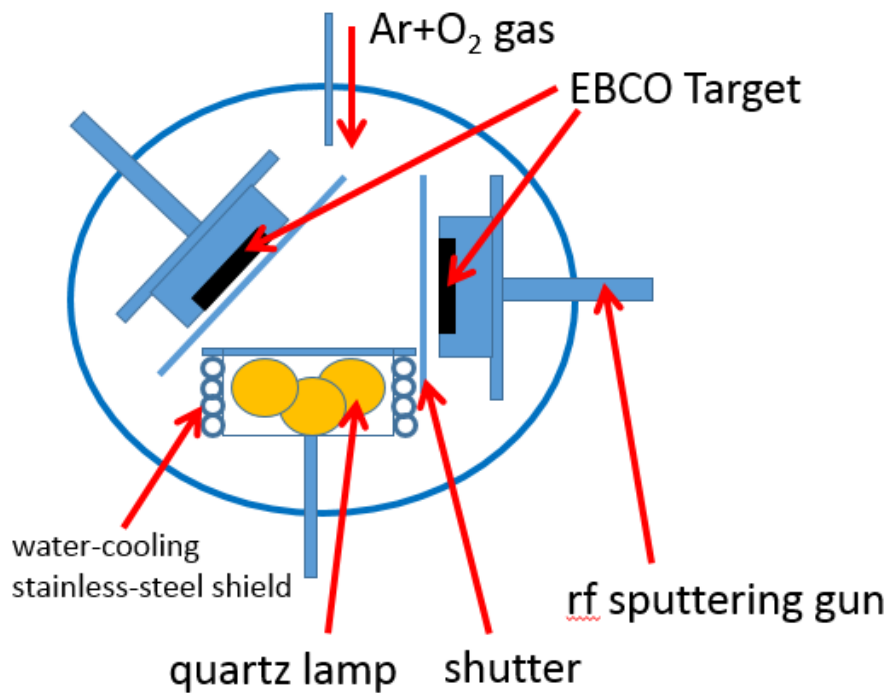
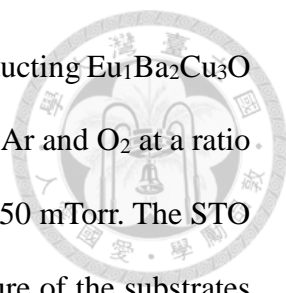


Figure 3.1.1: A schematic of the RF sputtering system.

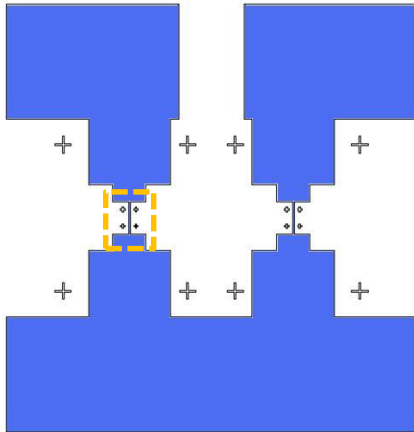


Two 2-inch in diameter targets made of stoichiometric superconducting  $\text{Eu}_1\text{Ba}_2\text{Cu}_3\text{O}$  compound were installed in the RF sputtering chamber. A mixture of Ar and  $\text{O}_2$  at a ratio of 9 ( $\text{Ar}/\text{O}_2$ ) was used as the sputtering gas at the pressure of about 350 mTorr. The STO substrates were mounted on the quartz holder. The growth temperature of the substrates was controlled by three 1kW quartz lamps underneath the holder. The growth time of the EBCO films was two hours by activating two 50W RF sputter guns. The post-growth annealing time is approximately 1 hour at the same deposition output power of three 1kW quartz lamps. The profile of the cooling process consists of two stages: (1) the temperature was cooled down to  $250^\circ\text{C}$  from the deposition temperature at the rate of  $5^\circ\text{C}/\text{min}$ , (2) followed by a rate of  $15^\circ\text{C}/\text{min}$  down to the room temperature.

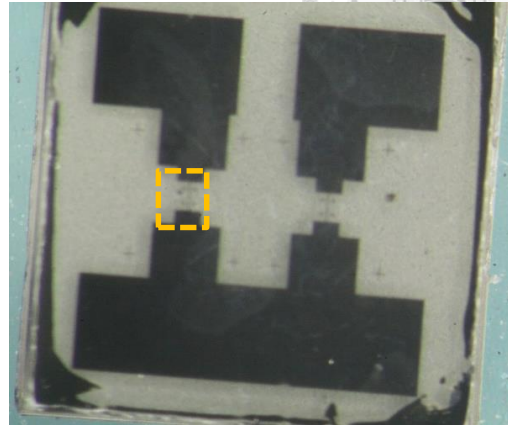
## 3.2 Fabrication of SNS devices

Once the growth of EBCO thin film on STO was completed, the fabrication of the EBCO/Au/EBCO devices shown in figure 3.2.2 was followed. Extra care should be exerted at each step to ensure the successful fabrication of the SNS devices since no one had ever tried it at the time. We patterned our EBCO thin film as shown in figure 3.2.1 (b) by photolithography. Figure 3.2.1 (a) is a schematic of our mask, and (b) is the SEM image for the region that circled by dotted line in (a) and (b). The edge accumulation was observed during the fabrication since the size of the STO substrate was about  $3.3 \times 3.3 \text{ mm}^2$ ; too small for a homogeneous spin coating. Nevertheless, it would not affect the results of the electrical characterization.

(a)



(b)

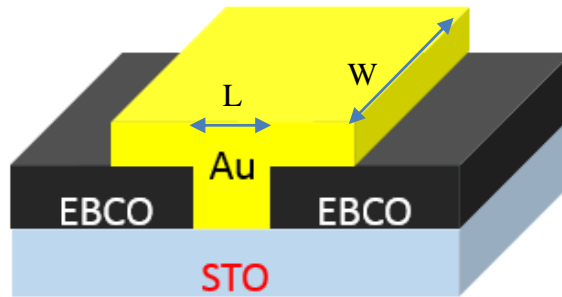


(c)

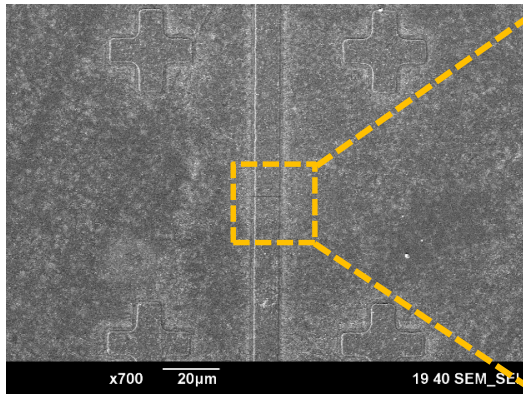


Figure 3.2.1: Optical lithography technique for the SNS device. (a) Mask. (b) Patterned EBCO thin film on STO. (c) The SEM image for the superconductor bridge is the region that circled by dotted line in (a) (b).  $W$  is the width of bridge,  $W \sim 10 \mu\text{m}$ .

(a)



(b)



(c)

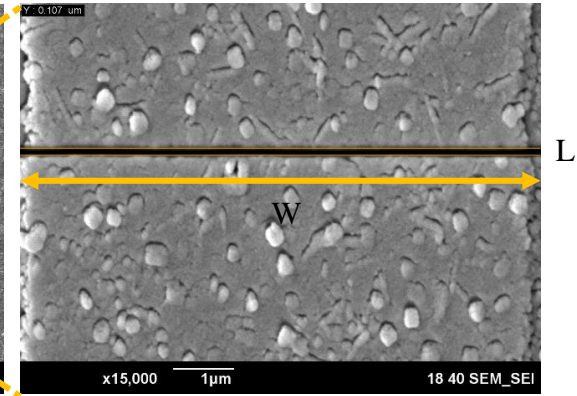


Figure 3.2.2: (a) Shows the schematic of the EBCO/Au/EBCCO structure, (b) is the SEM diagram of the EBCO bridge cut by focus ion beam (FIB), and (c) is the SEM image of the squared region in (b), where  $W$ ,  $\sim 10 \mu\text{m}$ , is the width of bridge, and  $L$ ,  $\sim 107 \text{ nm}$ , is the length of the gap.

The focus ion beam (FIB) was employed to cut the superconducting bridge as shown in figures 3.2.2 (b) and (c) after patterning the EBCO thin film. The depth of each cut is  $1 \mu\text{m}$ , which will assure the separation of the EBCO on both sides of the bridge from each other. Before the deposition of Au to fill up the region cut by FIB, a thermal annealing is needed to recover the damaged structure in the EBCO film by the  $\text{Ga}^+$  during the FIB process and to evacuate the inevitably implanted  $\text{Ga}^+$  ion. Figure 3.2.2 (a) illustrates the final structure of the EBCO bridge device.



### 3.3 Fabrication of SGS devices

In the bridge structure, the Au contact can be replaced by graphene to form SGS devices. Exfoliated graphene was used for the purpose of feasible fabrication of EBCO/graphene/EBCO structure. Most of the SGS devices were done in an opposite fashion as shown in figure 3.3.1 (a); depositing superconductors on the graphene thin film transferred onto the Si/SiO<sub>2</sub> substrate. The reason why we reversed the process was due to the high-temperature superconductors used for investigation. Unlike metallic superconductors, the growth of high-temperature superconductors needs a lattice-matched substrate. This is why EBCO was positioned under graphene.

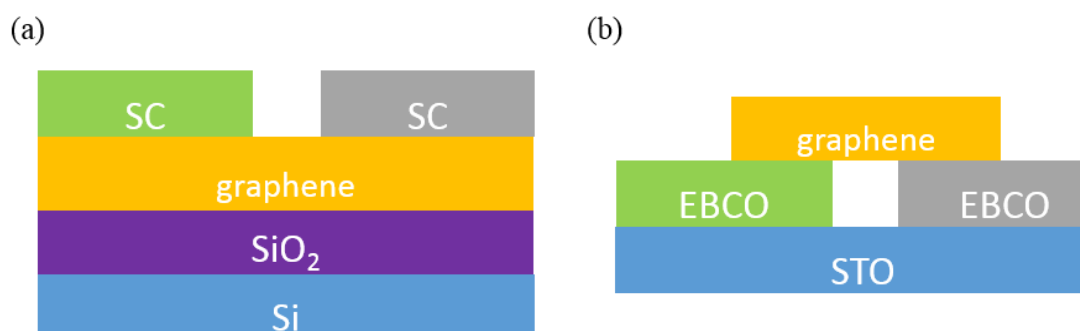


Figure 3.3.1: Shows a schematic representation of different structures of SGS devices; (a) structure previously used for metallic superconductors, and (b) a novel device structure for high-temperature superconductors, where SC is the abbreviation of superconductor.

### 3.4 Four-terminal resistance measurement



The four-terminal resistance measurement is a common technique for the high accuracy, especially in cryogenic experiments. This technique can minimize the measurement errors caused from the contact resistance. If we perform a two-terminal measurement, the contact resistance would usually severely compromise the measuring results; therefore, we chose a four-terminal resistance measurement. However, the resistance measured by the four-terminal resistance measurement method are obtained from the van der Pauw method.

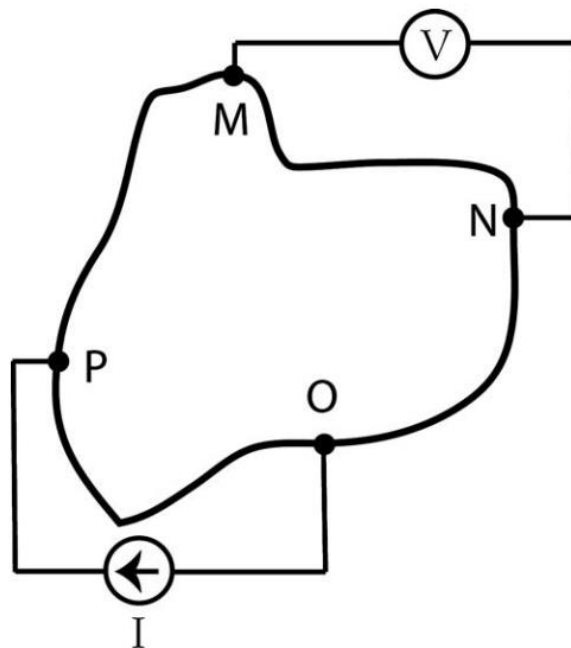
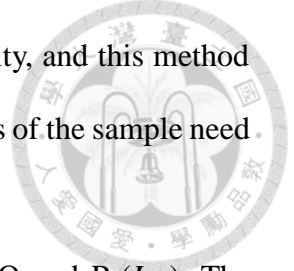


Figure 3.4.1: The configuration for van der Pauw method with an arbitrary shape and four contacts located at the peripheral. The resistance  $R_{MN,OP}$  is measured across contacts M and N, and the current source is passing through contacts O and P. [1].

The van der Pauw method is usually used for measuring the resistivity, and this method can be applied to any sample with an arbitrary shape, but the thickness of the sample need to be uniform and the area of contacts should be as small as possible.



As shown in figure 3.4.1, current will pass through contacts O and P ( $I_{OP}$ ). The potential difference between contacts M and N ( $V_{MN}$ ) is measured. By Ohm's law, the resistance between contacts M and N can be found as in eq. (3.4.1).

$$R_{MN,OP} = \frac{V_{MN}}{I_{OP}} \quad (3.4.1)$$

$R_{MN,OP}$  is a resistance between contact M and N. By van der Pauw formula [4], the relation between resistances can be expressed as the following

$$e^{-\frac{\pi d R_{MN,OP}}{\rho}} + e^{-\frac{\pi d R_{NO,PM}}{\rho}} = 1 \quad (3.4.2)$$

where  $d$  is the sample thickness and  $\rho$  is the resistivity of the sample.

For our measurement, a high resistance resistor ( $\sim 100 \text{ M}\Omega$ ) was connected to the sample in series., as shown in figure 3.4.2. The longitudinal resistance  $R_{xx}$  and Hall resistance  $R_{xy}$  are defined as:

$$R_{xx} = V_{xx} / I_{SD}$$

and

$$R_{xy} = V_{xy} / I_{SD},$$

where  $V_{xx}$  and  $V_{xy}$  are the electric potentials parallel and perpendicular to the direction of source-drain current, respectively.

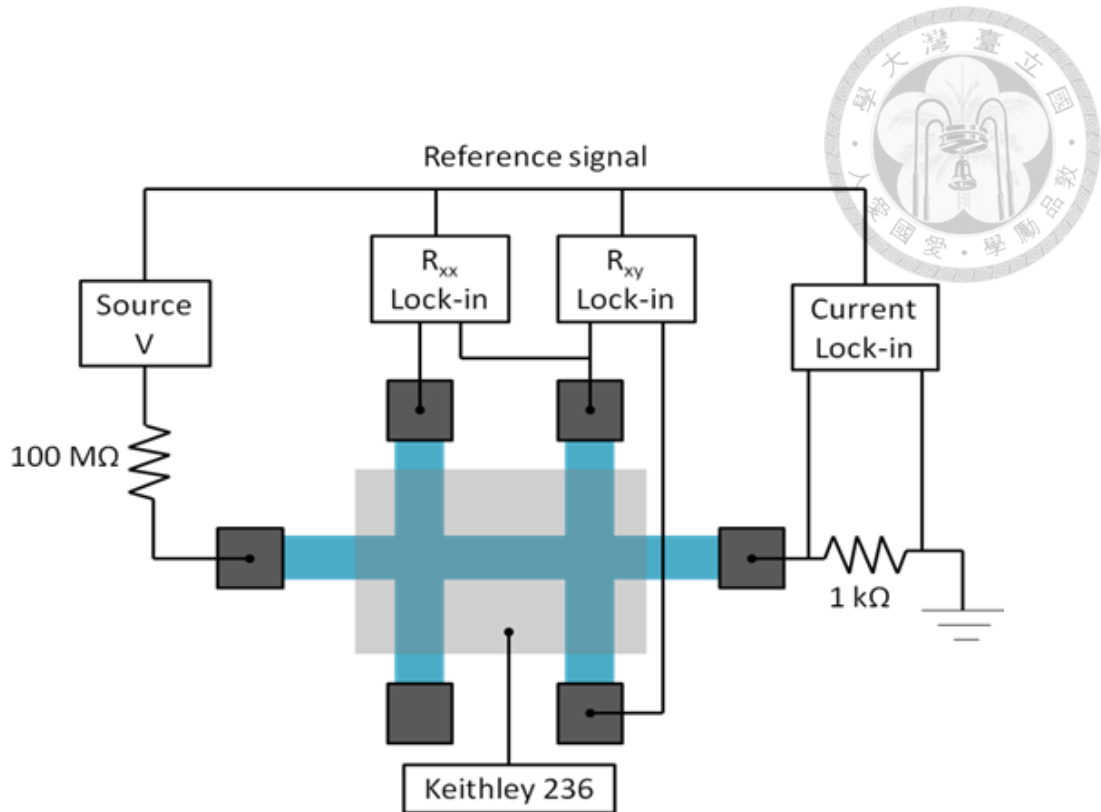


Figure 3.4.2: The configuration of four-terminal measurement [2].

### 3.5 Cryogenic system: Sorption pumping $^3\text{He}$ cryostat

In order to measure the sample at the low temperature, a top loading  $^3\text{He}$  cryostat from Oxford Instrument, as show in figure 3.5.1, was utilized. The maximum magnetic field is about 15 Tesla at the temperature of approximately 0.3 K. The condensation of  $^3\text{He}$  gas, as shown in figure 3.5.2, can cool the temperature down to 1.2 K. By lowering the vapor pressure of liquid  $^4\text{He}$  in the 1K pot, which can be kept at around 2 K below the boiling point of helium. Then, warming up the sorb to 30 K to release  $^3\text{He}$  gas stored from the sorb into the sample space. That is the condensation of  $^3\text{He}$ .

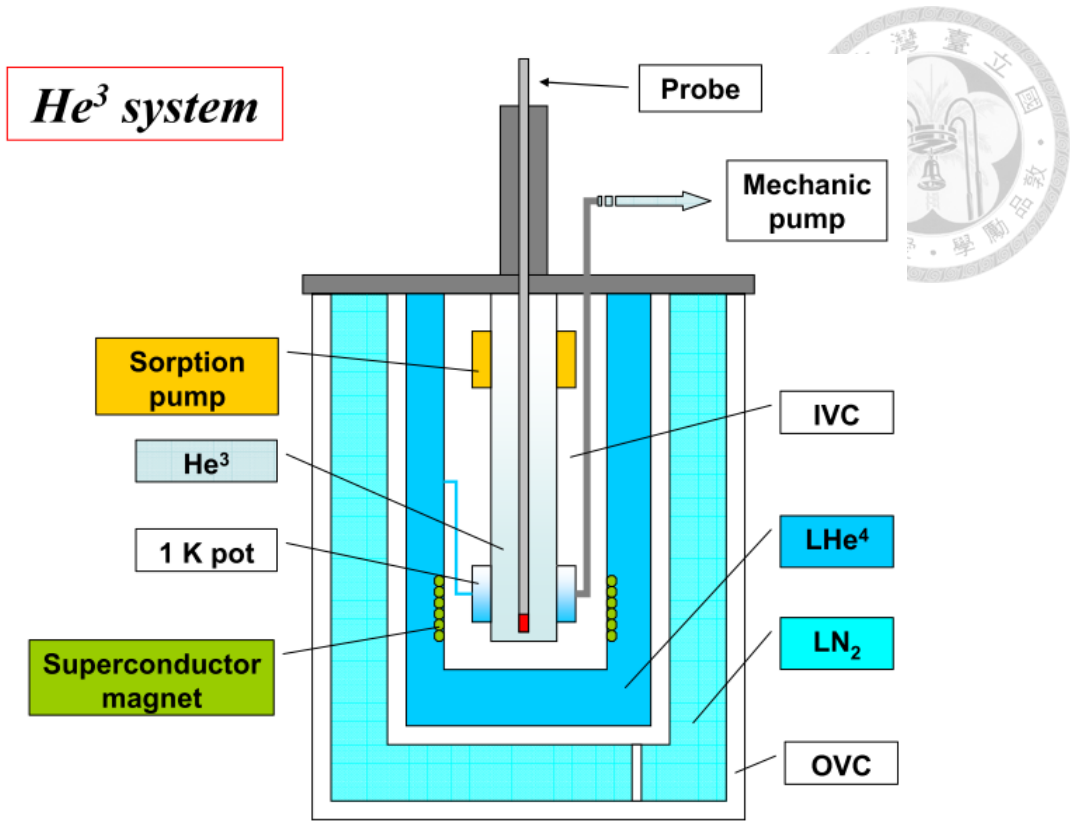


Figure 3.5.1: Shows a schematic diagram of Oxford instrument [3].

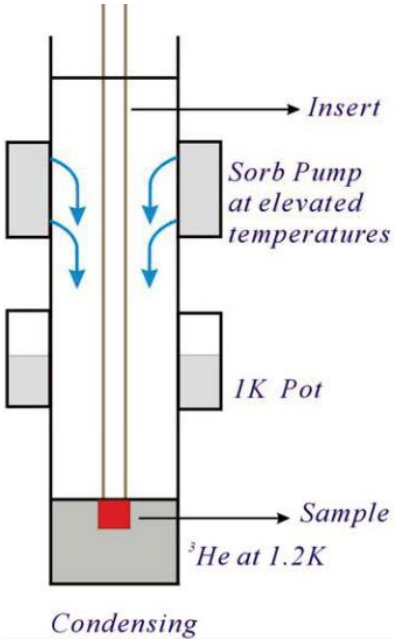


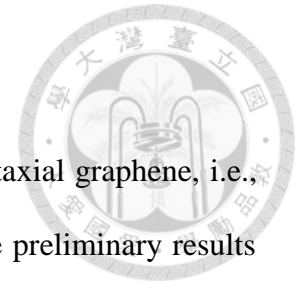
Figure 3.5.2: The process of  $^3\text{He}$  condensation. It shows releasing of  $^3\text{He}$  gas [4].

## References



- [1] S. H. N. Lim, D. R. McKenzie, and M. M. M. Bilek, *Rev. Sci. Instrum.* **80**, 075109 (2009).
- [2] Jheng-Cyuan Lin, Master thesis, National Taiwan University (2012).
- [3] Jyun-Ying Lin, Master thesis, National Taiwan University (2006).
- [4] Tzu-Lun Lin, Master thesis, National Taiwan University (2009).

## Chapter 4 Results of epitaxial graphene

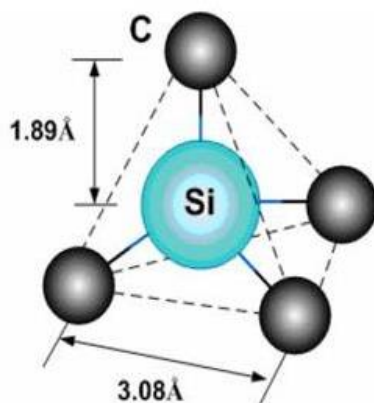


This part of thesis will discuss the experimental results of epitaxial graphene, i.e., the electric properties of graphene grown on the SiC substrate. The preliminary results showed weak localization, current heating, and insulator-quantum Hall transition in the epitaxial graphene. The fundamentals of these findings will be introduced first; followed by the experimental results.

### 4.1 Characteristics of epitaxial graphene

At first, we should know how graphene can grow on SiC. Usually, epitaxial graphene can grow on two different faces of SiC, SiC (000 $\bar{1}$ ) carbon-terminated face (C-face) or SiC (0001) silicon-terminated face (Si-face) [1, 2]. Our epitaxial graphene was grown on (0001) surface of 6H SiC, of which the structure is shown in figure 4.1.1.

(a)



(b)

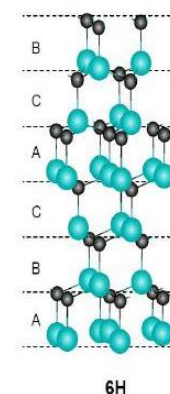


Figure 4.1.1: (a) the unit cell structure of SiC, (b) a kind of SiC polytypes, 6H. “6” refers to a stack of periodically arranged number (ABCACB), the letter “H” denotes the hexagonal symmetry of the SiC crystal. A and B only difference between shift of the lattice, their orientation do not change. But C means twisting the lattice by 60° [3].

It was easier to control the number of graphene layers grown on the Si-face than on the C-face because the growth of graphene on the Si-face is slower. For example, 2 monolayers of graphene were formed on Si-face after annealing at 1320 °C, but 16 monolayers on C-face at the same condition [4].

The epitaxial graphene was grown in a vacuum ( $10^{-6}$  torr) furnace by heating the SiC sample up to the temperature between 1100 °C and 1600 °C to form the graphene layer due to the sublimation of the Si atoms. This method provided a graphene layer with higher quality and more uniform film, as well as large area graphene layer, than the CVD graphene on Cu.

#### 4.1.1 Weak localization

The collision of electrons with particles while moving can be elastic or inelastic. In general, when the temperature is increased, the increased number of phonons will raise the chance of inelastic scatterings between electrons and phonons; destroying the coherence of the wave function of electrons; In contrast, when the temperature is lowered, the effect of inelastic scattering with phonons will be reduced. At the same time, the elastic scattering will be enhanced; without energy loss or momentum change. An interesting quantum effect, known as weak localization, can be observed.

We consider electrons transport in a system with impurities at low temperatures without external magnetic field, as shown in figure 4.1.2. It is no doubt that  $C=C'$  in time reversal symmetry, in the classical case, electron appear at origin O is no different between clockwise path and counter-clockwise path, i.e. electron maybe appear at origin O by two different trajectories; if we consider the quantum mechanics, then, we can write

the down the equation of total probability density between A and B is given by [5]

$$P_{[A,B]} = \sum_{i,j} A_i A_j^* = \sum_i |A_i|^2 + \sum_{i,j,i \neq j} A_i A_j^* \quad (4.1.1)$$

where  $A_i, A_j$  are amplitudes of probability. The first term we know that it is the same result as classical case, and second term is interference phenomenon in quantum case, moreover, the phase of electrons are random, so the second term which sum over different phase between two electrons will be zero. However, there is no phase difference and no different path between two electrons come from to origin O, because of elastic scattering, so we can re-write eq. (4.1.1) to

$$P_{[A,A]} = \sum_{i,j} A_i A_j^* = \sum_i |A_i|^2 + \sum_i A_i A_i^* = 2 \sum_i |A_i|^2 \quad (4.1.2)$$

we can clearly find that the eq. (4.1.2) shows twice probability density than classical result in eq. (4.1.1), simply to say, we will see the resistivity lager than classical result, the quantum effect called weak localization. So if we break the phase coherence of electron, like applied magnetics or increased temperature, the weak localization will be suppressed.

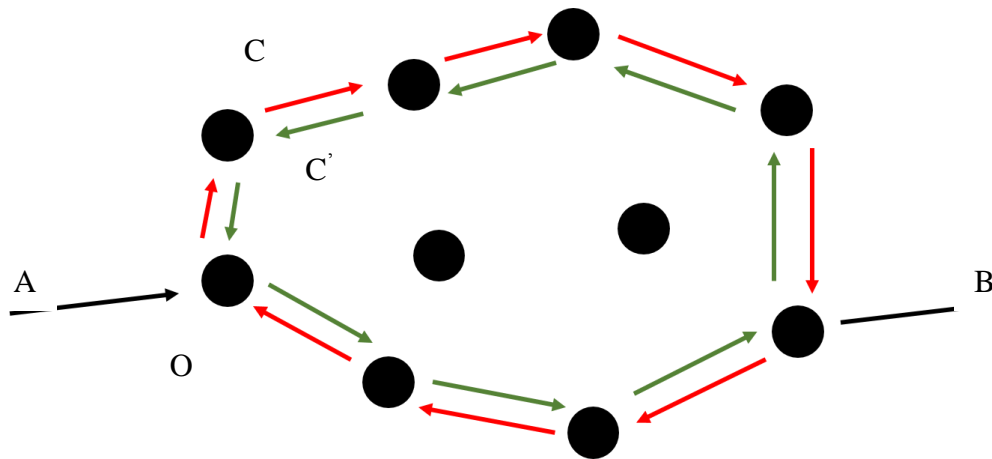
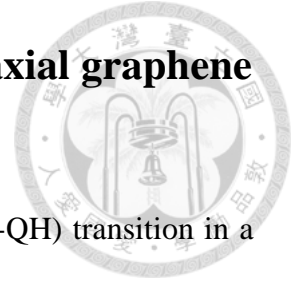


Figure 4.1.2: A schematic shows the time reversal trajectory of electrons between A and B, where O is the origin, C and C' denote the amplitudes of the wave functions of electrons moving clockwise and counter-clockwise, respective [6, 7].

## 4.2 Insulator-quantum Hall transition in epitaxial graphene



The experimental evidence of direct insulator-quantum Hall (I-QH) transition in a multi-layer graphene was revealed [8]. In this thesis, the I-QH transition in epitaxial graphene was observed as illustrated in figure 4.2.1, showing the change of resistivity  $\rho_{xx}(B)$  at different temperatures with a magnetic field varying from 0.1 T to -1.7 T. The critical magnetic field ( $B_c$ ) at -1.286 T was observed in figure 4.2.1. The temperature dependence of  $\rho_{xx}(B)$  was reversed around  $B_c$ ; at which the I-QH transition occurred.

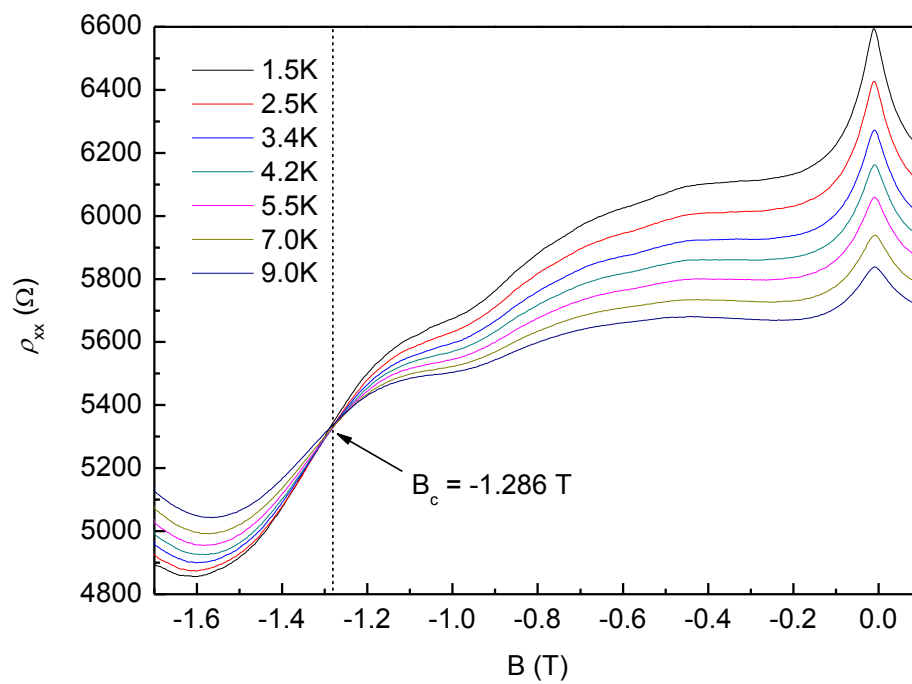


Figure 4.2.1: The curves of  $\rho_{xx}$  at different temperatures in high-field I-QH transition.

A theoretical model is needed to interpret the evidence of I-QH transition observed in figure 4.2.1. Universal scaling theory, which usually was used to check whether this kind of transitions are real phase transition [9], can be used to verify the I-QH transition.

The longitudinal resistivity can be denoted as

$$\rho_{xx} = f[(B - B_c)T^{-\kappa}], \quad (4.2.1)$$

near the transition point we get

$$|d\rho_{xx}/dB|_{B=B_c} \propto T^{-\kappa}, \quad (4.2.2)$$

where  $\kappa$  denotes the critical exponent.

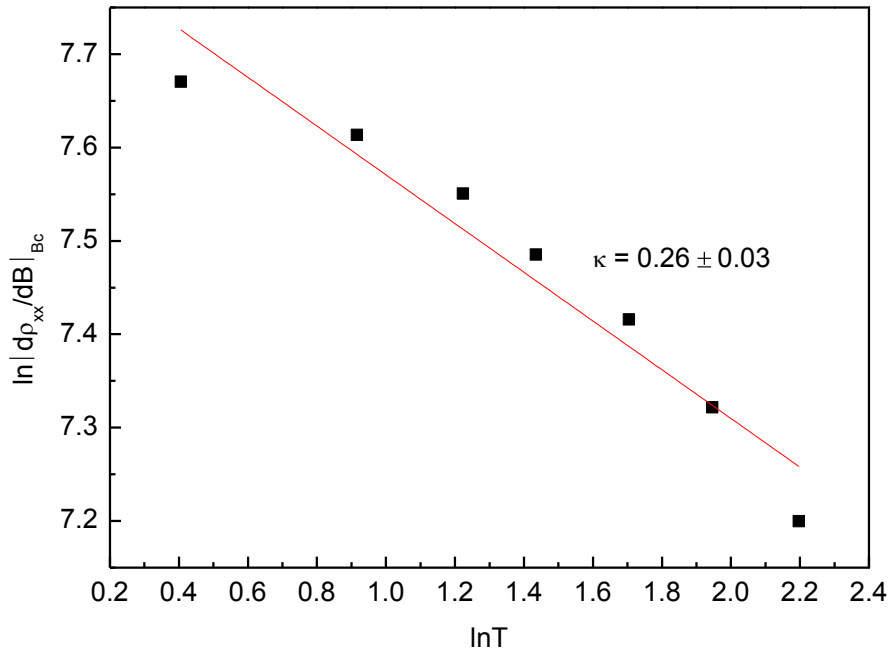
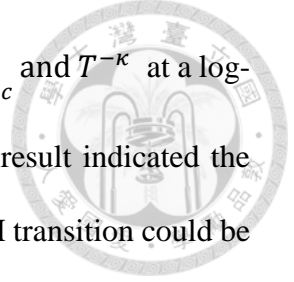


Figure 4.2.2: The diagram of  $\ln |d\rho_{xx}/dB|_{B_c}$  vs  $\ln T$ . From the slope, we obtain the scaling exponent  $\kappa \approx 0.26$ .

Figure 4.2.2 indicates a linear relationship between  $\ln \left| \frac{d\rho_{xx}}{dB} \right|_{B=B_c}$  and  $T^{-\kappa}$  at a log-log scale; where the critical exponent  $\kappa \cong 0.26$ . The experimental result indicated the behavior of a conventional two-dimensional electron gases. The I-QH transition could be attributed to the spin-degenerate Landau levels and dominant short-range disorder [10].



### 4.3 Weak localization and electron heating in epitaxial graphene



In this section, we want to study two different scattering mechanisms, electron-phonon and electron-electron scatterings, in a two-dimensional electron system by current heating effect. In general, it is difficult to study these two different scattering mechanisms independently in a two-dimensional electron system. When the electron effective temperature ( $T_e$ ), heated by a current or an electric field, is considerably larger than the lattice temperature ( $T_L$ ), it was known as the current heating effect. In this study, the weak localization was utilized as a thermometer for the measurement of  $T_e$ ; showing that current heating effect is a powerful tool for the studies of nanodevices.

First part, we use the weak localization effect as thermometer to calculate  $T_e$  [11]. Figure 4.3.1 shows the relationship between the magnetoresistance and the applied magnetic fields, in the epitaxial graphene at different temperatures. The magnetic field is from -1 tesla to 1 tesla ( $B = -1\text{T} \sim B = 1\text{T}$ ), and the temperature is between  $T = 1.95\text{ K}$  and  $T = 25\text{ K}$ . The negative magnetoresistance indicates the presence of the weak localization. We can use the resistance peak value, decreasing with the increasing temperature, of the weak localization effect as a thermometer to calculate  $T_e$ .

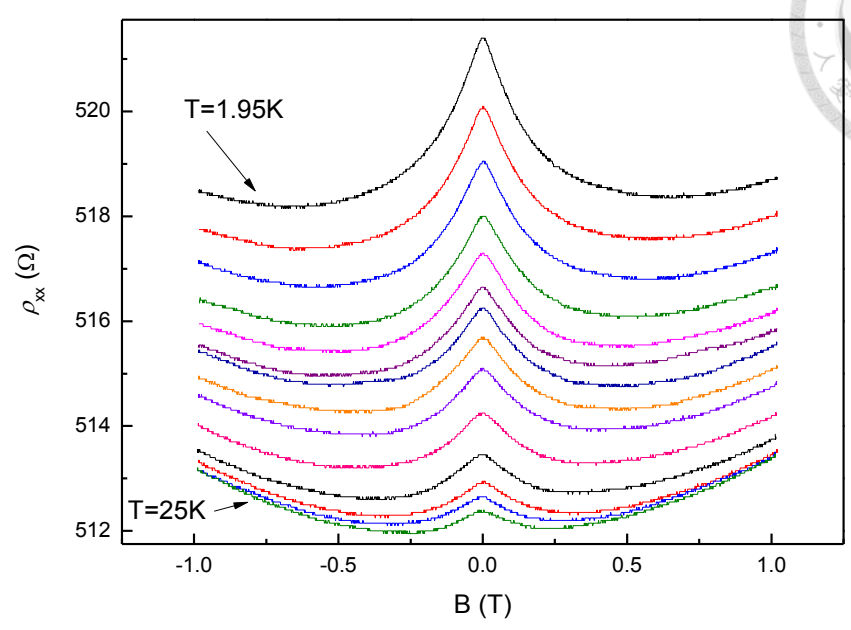


Figure 4.3.1: Depicts the results of weak localization observed in an epitaxial graphene in the low magnetic field at different temperatures.

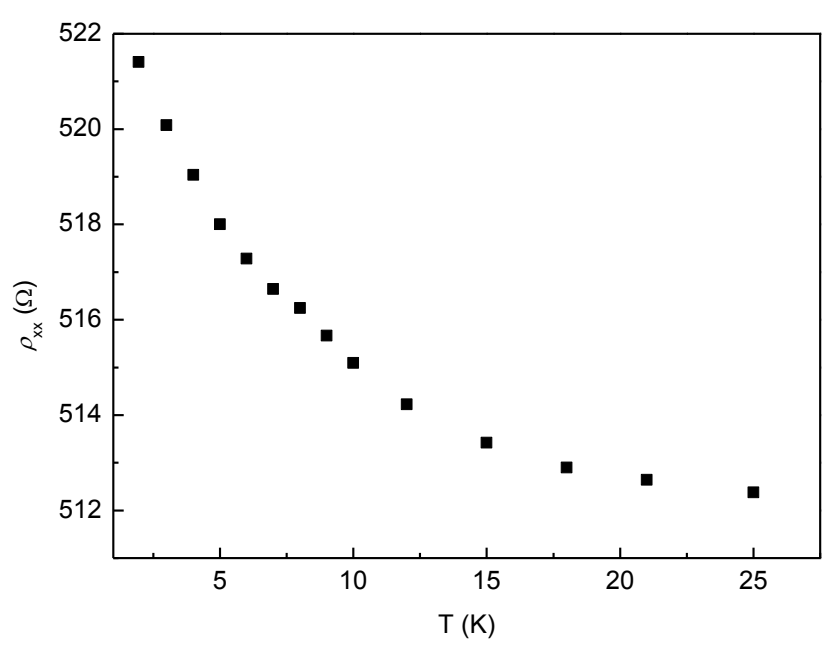


Figure 4.3.2: Shows the resistivity  $\rho_{xx}$  as a function of temperature.

The relationship between the resistance peak and the temperature in figure 4.3.1 is rearranged in figure 4.3.2, showing a better visualization of the temperature dependence on the measured resistivity. Figure 4.3.3 shows the results of the weak localization effect in the epitaxial graphene at the low magnetic field by varying the current. In order to clearly observe the phenomenon, the temperature dependence of the peak resistivity was shown in figure 4.3.4, in which the temperature was fixed at 1.95 K ( $T_L = 1.95$  K), and the injecting current was varied between  $I = 2 \mu\text{A}$  and  $I = 225 \mu\text{A}$  to achieve the heating effect. When the applied current  $I > 20 \mu\text{A}$ , the resistivity is a function of the injecting current. If the applied current,  $I < 10 \mu\text{A}$ , the peak resistivity and the applied current are independent, i.e., the current heating effect can only be observed in the high injecting current region.

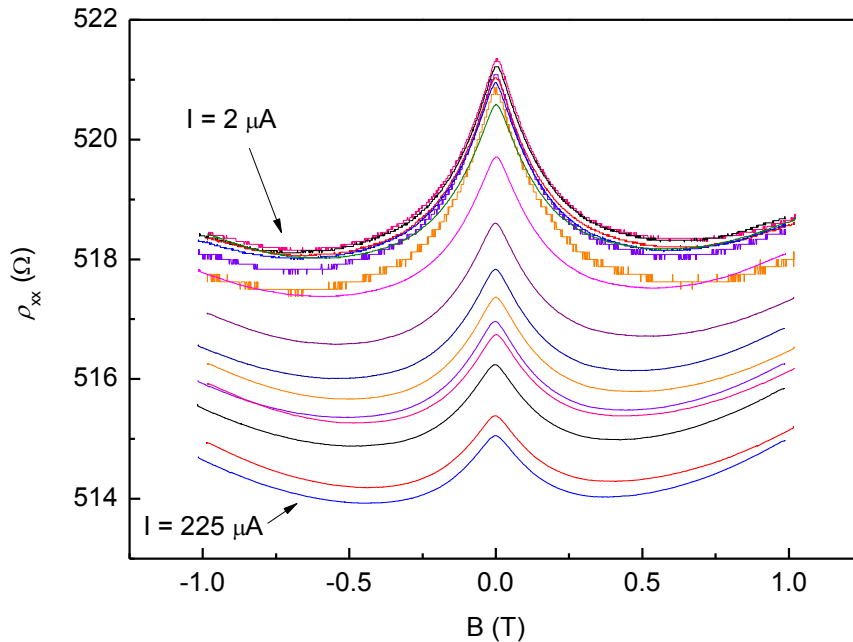


Figure 4.3.3: Weak localization of epitaxial graphene in the low magnetic field with

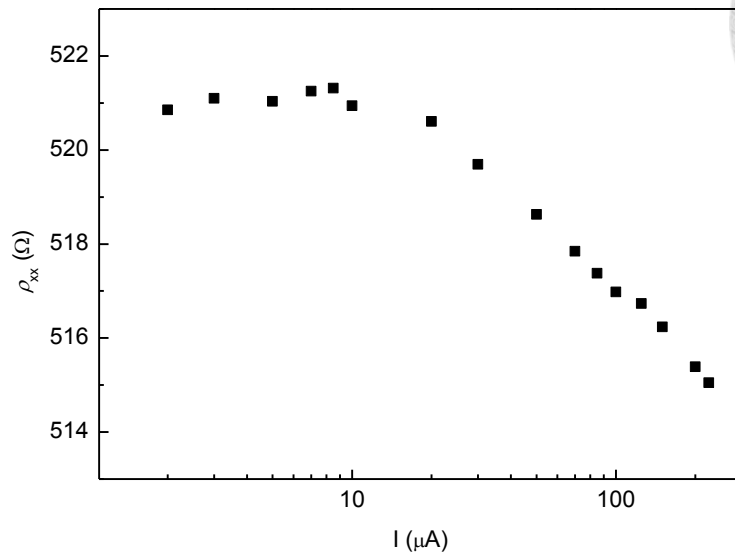


Figure 4.3.4: Shows resistivity  $\rho_{xx}$  linear dependence on the increasing temperature.

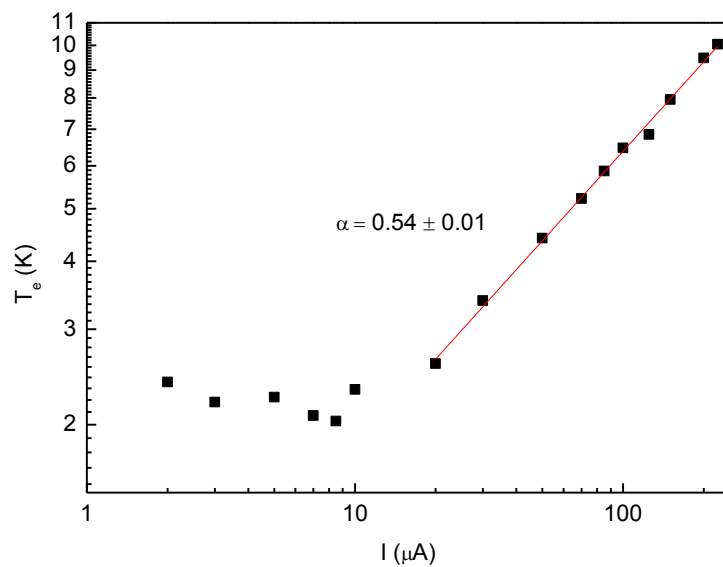


Figure 4.3.5: Shows the electron effective temperature  $T_e$  as a function of current  $I$  at  $T = 1.947$  K in a logarithmic scale. The linear line represents a power law  $T_e \propto I^\alpha$  with the exponent  $\alpha = 0.54$ . When the current is below  $10 \mu\text{A}$ , we cannot observe the dependence between  $T_e$  and  $I$ ; on the contrary, we observe the linear dependence at high current ( $I > 20 \mu\text{A}$ ).

From figure 4.3.5, it is observed that  $T_e$  is a function of the injected current at higher current values ( $I > 20 \mu\text{A}$ ); therefore, we could use the weak localization effect as a thermometry to measure the electron effective temperature  $T_e$  by interpolation.

In Figure 4.3.5, we found the relation of  $T_e \propto I^{0.54}$ . Applying the work by Scherer and co-workers [12] on our data, the inelastic scattering length is given by

$$l_{in} \sim T^{-p/2}, \quad (4.3.1)$$

where  $p$  is an exponent related to inelastic scattering. The Fermi distribution function was characterized by  $T_e$  and it is given by the energy acquired by the electron diffusing distance,  $l_{in}$ , in an electric field  $E$  [13]; therefore,

$$k_B T_e \sim e E l_{in}. \quad (4.3.2)$$

By inserting eq. (4.3.1) and  $E \sim I$  into eq. 4.3.2 leads to

$$T_e \sim I^{2/(2+p)}. \quad (4.3.3)$$

In our result, the exponent  $\alpha = 0.54$ , therefore  $p$  is  $\sim 1.7$ , which is similar to the results published by other groups [12, 14]. Moreover, our exponent  $p$  approximately equals to 2, meaning that the scattering mechanism of our system should be electron-phonon scattering ( $\frac{1}{\tau_{ep}} \propto T^2$ ), which will introduce inelastic scattering between electron and phonon, where  $\tau_{ep}$  is electron-phonon scattering rate [12].

In this part, we can observe the current heating effect in epitaxial graphene from another perspective. First, we should transform the data from figure 4.3.1 to figure 4.3.6 by  $\Delta\rho_{xx}(B) = \rho_{xx}(B) - \rho_{xx}(B = 0)$ , it not only let us observe weak localization clearly, but also let us easily analyze the data by the following formula. In order to show how we fit the data, we select the data obtained at  $T = 3 \text{ K}$ , as shown in figure 4.3.7. The phase coherence length  $L_\phi$ , intervalley scattering length  $L_i$  and intravalley scattering length  $L^*$ , respectively, can be extracted by fitting the following equations [15]:

$$\Delta\rho(B) = -\frac{e^2\rho^2}{\pi h} \left[ F\left(\frac{B}{B_\phi}\right) - F\left(\frac{B}{B_\phi+2B_i}\right) - 2F\left(\frac{B}{B_\phi+B_*}\right) \right], \quad (4.3.4)$$

$$F(z) = \ln z + \psi\left(\frac{1}{2} + \frac{1}{z}\right), \quad B_{\phi,i,*} = \frac{\hbar c}{4e} L_{\phi,i,*}^{-2}, \quad (4.3.5)$$

where  $\psi(z)$  is the digamma function. This method can be only used for conventional weak localization to the resistivity and not the non-backscattering correction.

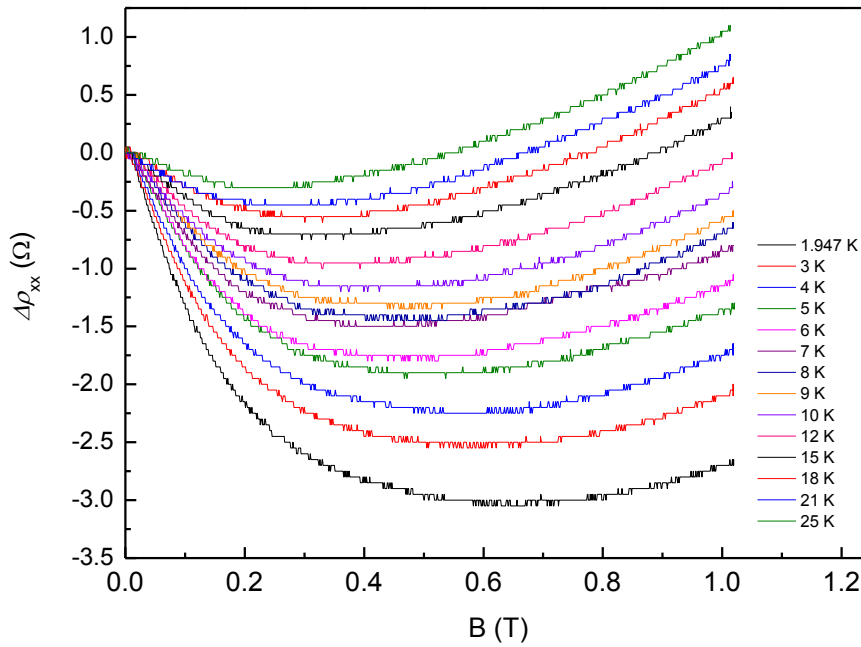


Figure 4.3.6: Shows the results of the weak localization in the low magnetic field at different temperatures. Curves are shifted such that the peak of WL peak is at 0 Ω. We can clearly observe the decreasing peak height of WL with the increasing temperature.

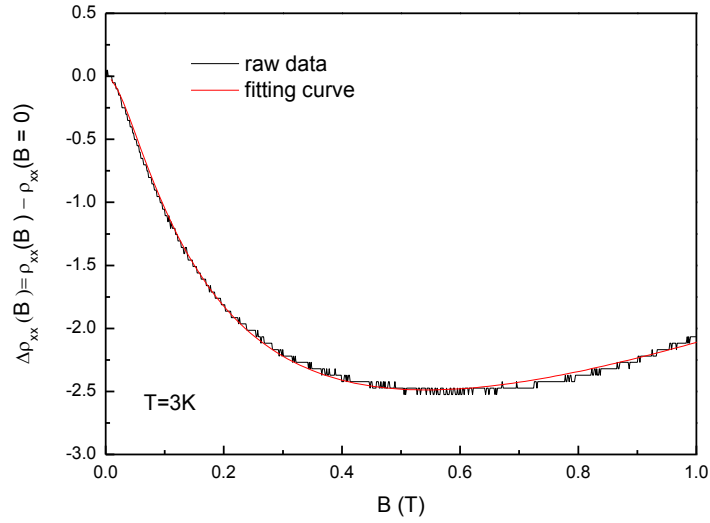
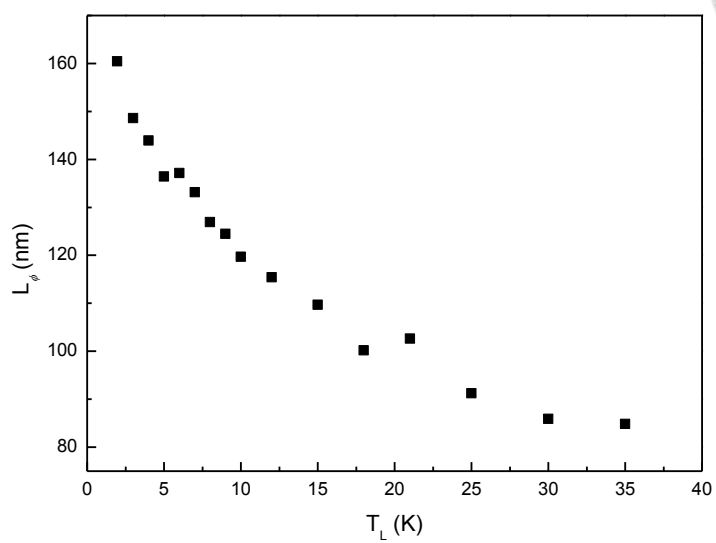


Figure 4.3.7: Shows a diagram  $\Delta\rho_{xx}(B) = \rho_{xx}(B) - \rho_{xx}(B = 0)$  (in black curve) vs. magnetic field  $B$ , the red curve is a fitting curve by eq. (4.3.3), at  $T = 3\text{K}$ .

Eq. (4.3.4) was used to fit the experimental results since it could analyze the relation between weak localization and temperature or that between weak localization and current heating; we will get some information by fitting, the value of phase coherence length ( $L_\varphi$ ), intervalley scattering length ( $L_i$ ) and intravalley scattering length ( $L^*$ ). In this thesis, we only considered the  $L_\varphi$  since our goal is to find out the relation between  $L_\varphi$  and temperature  $T$  or current  $I$ . Figure 4.3.8 (a) shows the relation between  $L_\varphi$  and temperature  $T$ . Figure 4.3.8 (b) depicts the relation between  $L_\varphi$  and current  $I$ . It can be seen that the coherence length  $L_\varphi$  decreased with the increasing temperature, as well as the linear dependence of the coherence length,  $L_\varphi$ , on the high injecting current region.



(a)



(b)

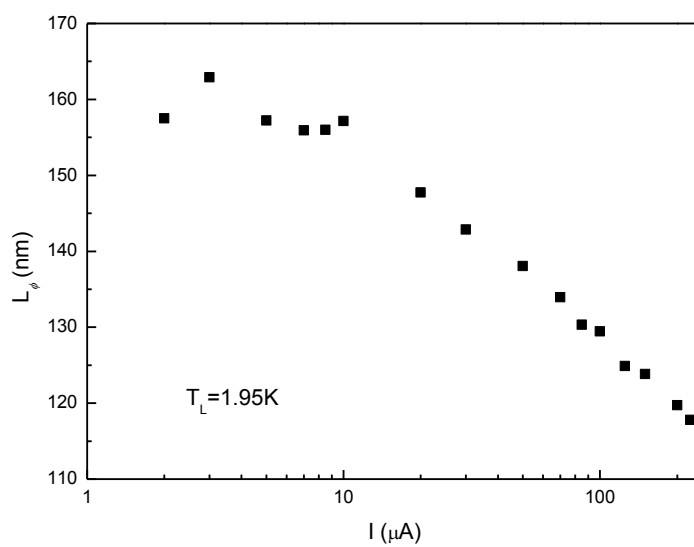
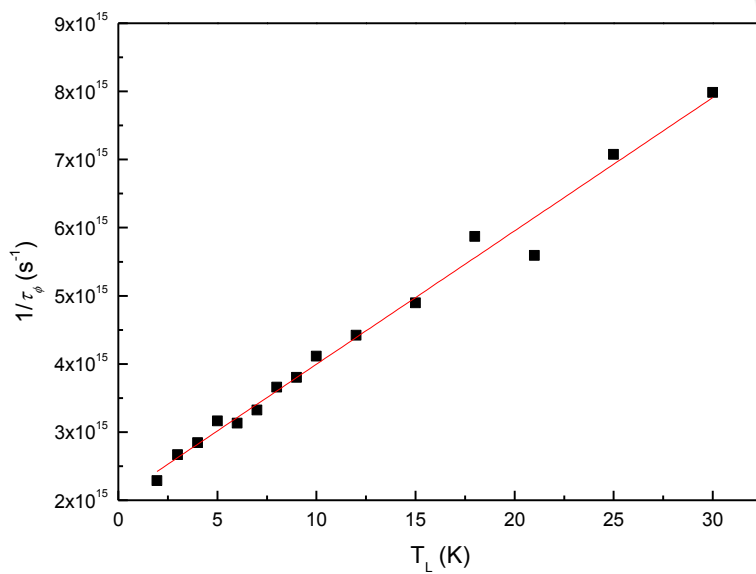


Figure. 4.3.8: (a) The lattice temperature dependence of the coherence length. (b) The current dependence of the coherence length.



(a)



(b)

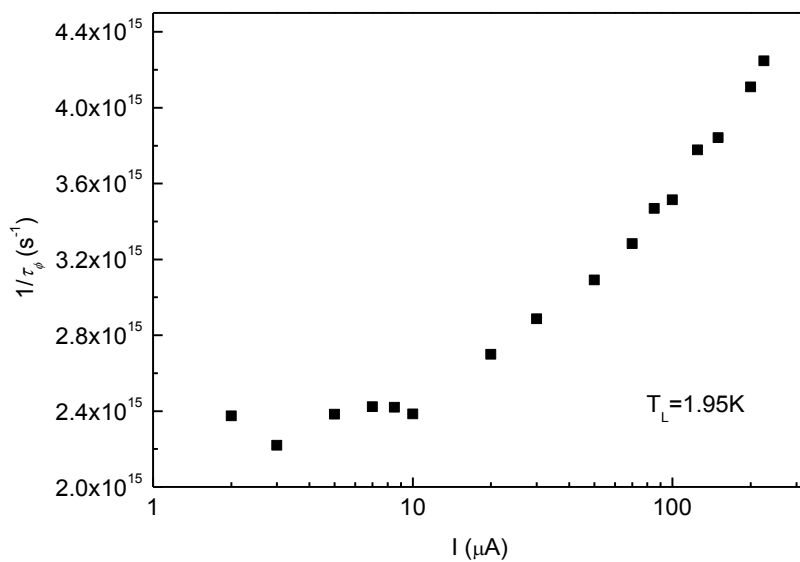


Figure 4.3.9: (a) The lattice temperature ( $T_L$ ) shows a linear dependence on the phase coherence rate ( $1/\tau_\phi$ ). (b) It shows current dependence of the phase coherence rate at a fixed temperature  $T_L = 1.95K$ .

Furthermore, the relation between phase coherence length  $L_\phi$  and phase coherence rate  $\tau_\phi$  (where  $\tau_\phi = L_\phi^2/D$ ,  $D$  is diffusion constant) can be used to observe the temperature and current dependence of phase coherence rate.

In figure 4.3.9 (a), we observed the linear temperature dependence of phase coherence rate ( $\frac{1}{\tau_\phi} = 2.13 \times 10^{15} + 1.85 \times 10^{14}T_L$ ). The result of the linear dependence shows the phase-breaking mechanism is caused by electron-electron scattering, instead of electron-phonon scattering, at low temperature [16]. In figure 4.3.9 (b), the phase coherence rate is independence of low injecting current; meaning the effective electron temperature  $T_e$  is equal to or less than the lattice temperature  $T_L$  ( $T_e \leq T_L$ , when current is low). We note that  $T_e$  can be considerably higher than  $T_L$  when a higher current was applied. Moreover, in order to calculate the effective electron temperature, we did the interpolation on the data in figure 4.3.9 (a) and (b).

In figure 4.3.9, the slope, i.e. exponent  $\alpha$ , of the straight line is equal to 0.48, which leads to  $p = 2.16$ . The result of  $p$  was also close to 2, indicating the electron-phonon scattering ( $\frac{1}{\tau_{ep}} \propto T^2$ ) in our system. The same results were derived by different methods, using the weak localization, as well as the phase coherence rate, as a thermometer for the extraction of the exponents  $\alpha$ , and  $p$ . Both of results suggested the electron-phonon scattering mechanism in our system.

In general, it is difficult to study electron-electron and electron-phonon scattering independently. By utilizing the electron heating effect, our experiments results suggested that the electron heating effect is a powerful tool for studying two inelastic scattering properties and physical phenomena in the two dimensional system or the nanostructures.

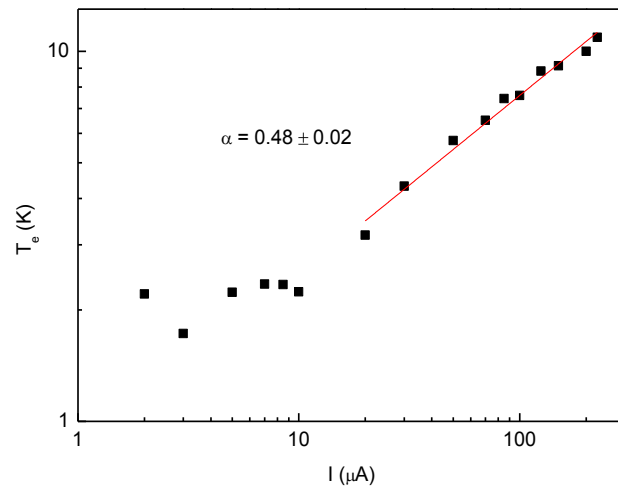


Figure 4.3.10: Shows the electron effective temperature  $T_e$  as a function of current  $I$  at  $T = 1.947\text{K}$ . The linear line represents a power law  $T_e \propto I^\alpha$  with the exponent  $\alpha = 0.48$ .

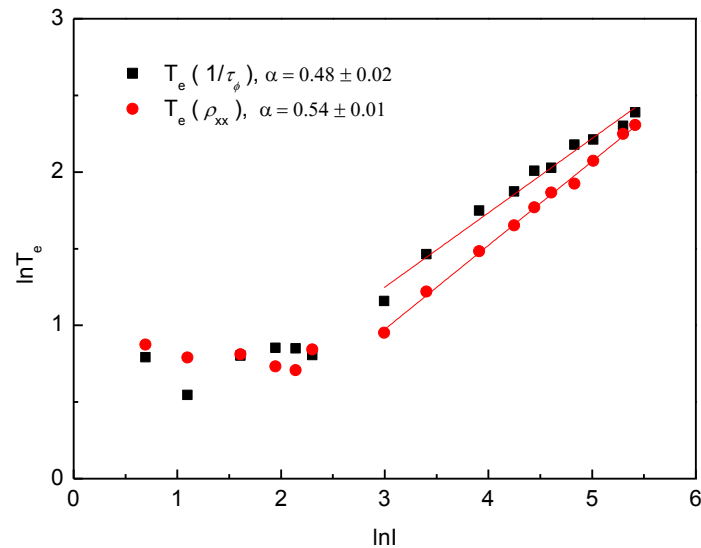


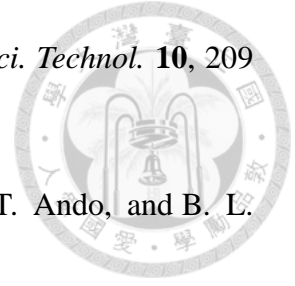
Figure 4.3.11: Illustrates the comparison of the results from two different analyses of the relationship between the injected current and the electron temperature in a logarithmic scale. The slopes of the straight lines obtained by the analyses of weak localization peak height and phase coherent rate are 0.54 and 0.48, respectively.

## References



- [1] Wataru Norimatsu, Juji Takada, and Michiko Kusunoki, *Phys. Rev. B* **84**, 035424 (2011)
- [2] Wataru Norimatsu, Michiko Kusunoki, *Chem. Phys. Lett.* **468** 52–56 (2009).
- [3] H. MorkoG, S. Strite, G. B. Gao, M. E. Lin, B. Sverdlov, and M. Burns, *J. Appl. Phys.* **76**, 1363 (1994).
- [4] N. Srivastava, Guowei He, Luxmi, P. C. Mende, and R. M. Feenstra, *J. Phys. D: Appl. Phys.* **45**, 154001 (2012).
- [5] P. M. Mensz and R. G. Wheeler, *Phys. Rev. B* **35**, 2844 (1987).
- [6] Tzu-Lun Lin, Master thesis, National Taiwan University (2009).
- [7] Kuang Yao Chen, Doctoral dissertation, National Taiwan University (2010).
- [8] Chiashain Chuang, Li-Hung Lin, Nobuyuki Aoki, Takahiro Ouchi, Akram M Mahjoub, Tak-Pong Woo, Jonathan P Bird, Yuichi Ochiai, Shun-Tsung Lo and Chi-Te Liang, *Nanoscale Res. Lett.* **8**, 214 (2013).
- [9] C. F. Huang, Y. H. Chang, C. H. Lee, H. T. Chou, H. D. Yeh, C.-T. Liang, Y. F. Chen, H. H. Lin, H. H. Cheng, and G. J. Hwang, *Phys. Rev. B* **65**, 045303 (2002).
- [10] H. P. Wei, S. W. Hwang, D. C. Tsui, and A. M. M. Pruisken, *Surf. Sci.* **229**, 34 (1990).
- [11] A. Mittal, R. G. Wheeler, M. W. Keller, D. E. Prober, and R. N. Sacks, *Surf. Sci.* **361/362** 537-541 (1996)
- [12] H. Scherer, L. Schweitzer, F. J. Ahlers, L. Blied, R. Losch, and W. Schlapp, *Semicond. Sci. Technol.* **10**, 963 (1995).
- [13] H. P. Wei, L. W. Engel and D. C. Tsui, *Phys. Rev. B* **50**, 14609 (1994)

- [14] S Koch, R J Haug, K von Klitzing and K Ploog, *Semicond. Sci. Technol.* **10**, 209 (1995).
- [15] E. McCann, K. Kechedzhi, Vladimir I. Fal'ko, H. Suzuura, T. Ando, and B. L. Altshuler, *Phys. Rev. Lett.* **97**, 146805 (2006).
- [16] K. K. Choi, D. C. Tsui, and K. Alavi, *Phys. Rev. B* **36**, 7751 (1987).



## Chapter 5 Results of SGS



In this chapter, we show the data about EBCO films, SNS, and SGS devices. First, the characteristics of EBCO films and the optimum condition at which EBCO on STO could be grown by RF sputtering will be shown; followed by the important characteristics of SNS and the results of the SGS device.

### 5.1 Experimental results of EBCO thin films

EBCO thin film was grown on  $\text{SrTiO}_3$  (STO) substrate by the RF sputtering system. The crystallization of EBCO thin film was examined by using X-ray diffraction (XRD) as shown in figure 5.1.1, and superconductivity properties by resistance-to-temperature measurement.

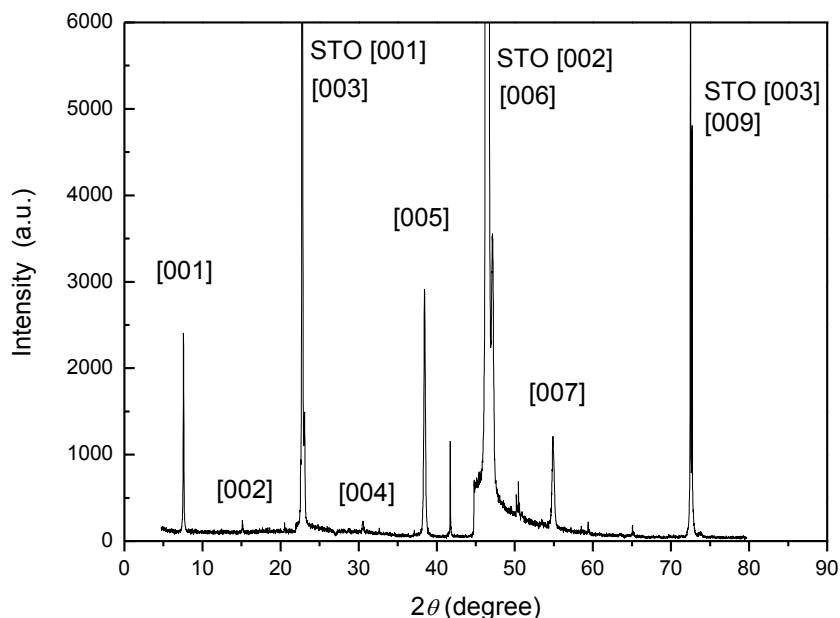
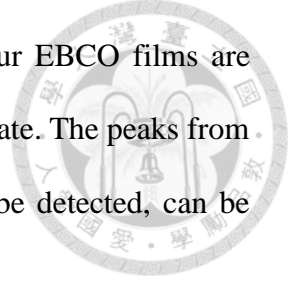


Figure 5.1.1: Shows the XRD diagrams of the EBCO thin film.

From the sharp peaks shown in figure 5.1.1, we knew that our EBCO films are monocrystalline. There are some peaks detected are from STO substrate. The peaks from [001] to [009], except [008] peak whose intensity is too small to be detected, can be clearly seen in figure 5.1.1.



In figure 5.1.2, the  $R-T$  curves of EBCO films show the zero-resistance when the experimental temperature is below its  $T_c$ . The best condition for the growth of EBCO films was found at pressure = 350 mTorr with the mixture of Ar and O<sub>2</sub> at a ratio of 9 (Ar/O<sub>2</sub>) and  $T = 575^\circ\text{C}$  for the deposition. The superconducting transition temperature of optimum EBCO thin film for the best deposition condition was around 91 K; approaching the historical records, 91 K ~ 93 K, of EBCO grown on STO by an RF sputtering system.

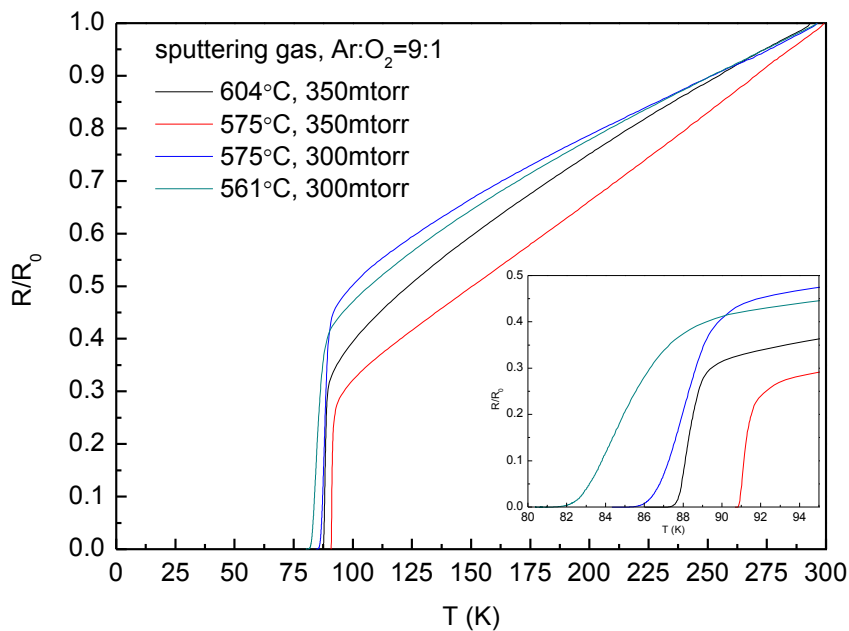
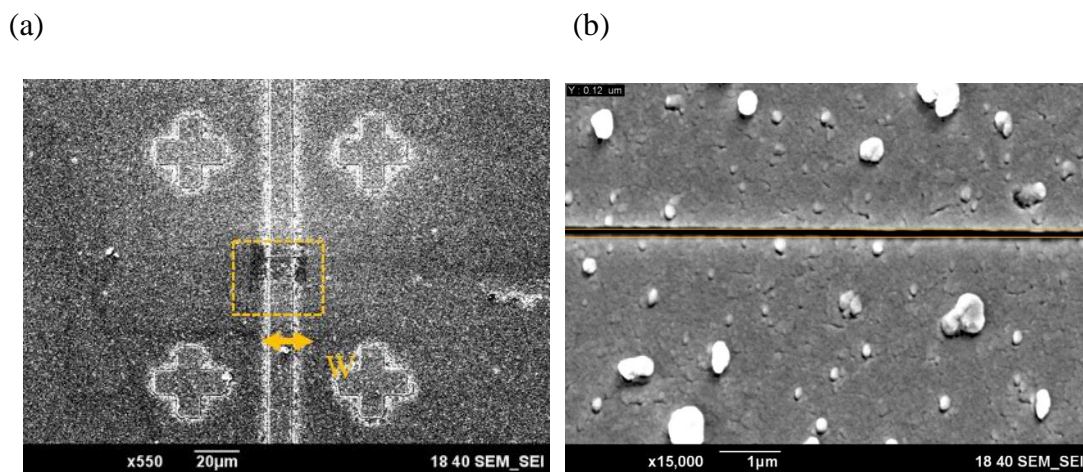


Figure 5.1.2: Shows the  $R-T$  diagrams of the EBCO thin films, at different temperature and sputtering gas pressure.



## 5.2 Experimental results of SNS

Extra care had been taken at each step to ensure the successful fabrication of the SNS devices since no one had ever tried the synthesis of EBCO/graphene/EBCO before. The fabrication of the EBCO/Au/EBCO devices was carried out after the growth of EBCO film on STO was optimized. The focus ion beam (FIB) was employed to make the superconducting bridge, separating the EBCO on both sides of the bridge from each other, as shown in figures 5.2.1. Then we recovered the damaged structure in the EBCO film by the  $\text{Ga}^+$  during the FIB process by thermal annealing. After the recovery of EBCO thin film, we deposited Au to fill up the cut, and we measure the junction by four-terminal measurements. Finally, the result was shown in figure 5.2.2.



Figures 5.2.1: (a) is the SEM diagram of the EBCO bridge cut by focus ion beam (FIB), where  $W$ ,  $\sim 10\mu\text{m}$ , is the width of the bridge, and (b) is the enlarged SEM image of the squared region in (a). The gap is about 120nm.

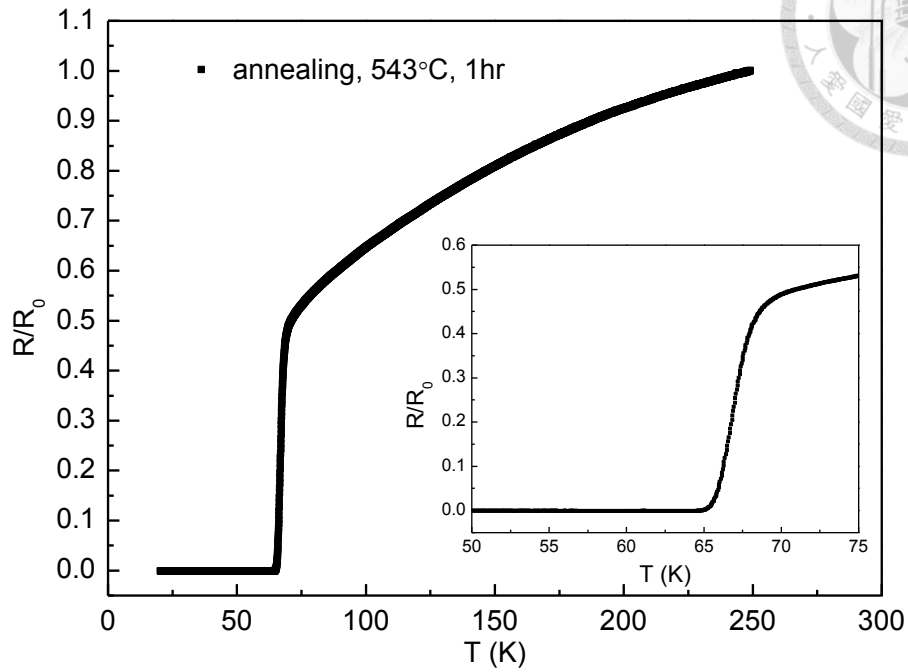
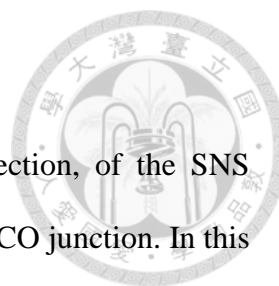


Figure 5.2.2: The  $R$ - $T$  diagram of the SNS sample.

In figure 5.2.2, we show the  $R$ - $T$  diagram of the EBCO/Au/EBCO sample. We observed the zero resistance in the junction. That means there are Cooper pairs tunneling across the EBCO bridge. After we deposited Au to fill up the cut, the device of EBCO/Au/EBCO was annealed at 543°C for an hour to improve the interface between EBCO and Au. Then it was cooled down to room temperature slowly at the rate of -5°C /min.



### 5.3 Experimental results of SGS

After the successful fabrication, discussed in the previous section, of the SNS devices, we tried to fabricate the unprecedented EBCO/graphene/EBCO junction. In this section, we show the experimental results of SGS.

Figure 5.3.1 shows the resistance-temperature ( $R$ - $T$ ) diagram of the EBCO electrodes in our SGS device. The inset to figure 5.3.1 is an enlarged picture to illustrate the zero resistance in the EBCO electrodes. In figure 5.3.2, we show the current-voltage ( $I$ - $V$ ) curve of the EBCO electrodes at  $T = 11\text{K}$ . The critical current can be found at around  $I = 50\text{ mA}$ . Both information means that superconducting behavior in our EBCO film existed. That is very important for the SGS device we fabricated.

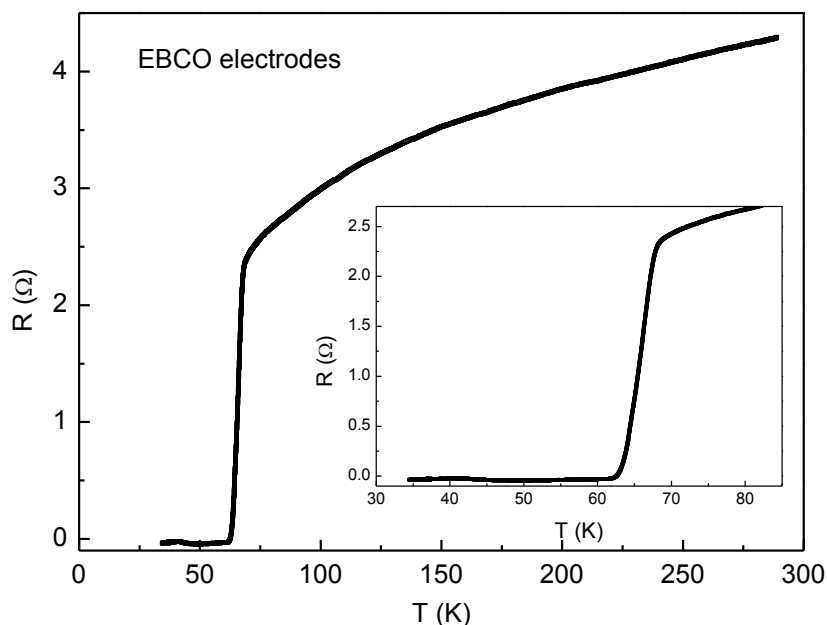


Figure 5.3.1: Shows the  $R$ - $T$  diagram of the EBCO electrodes.

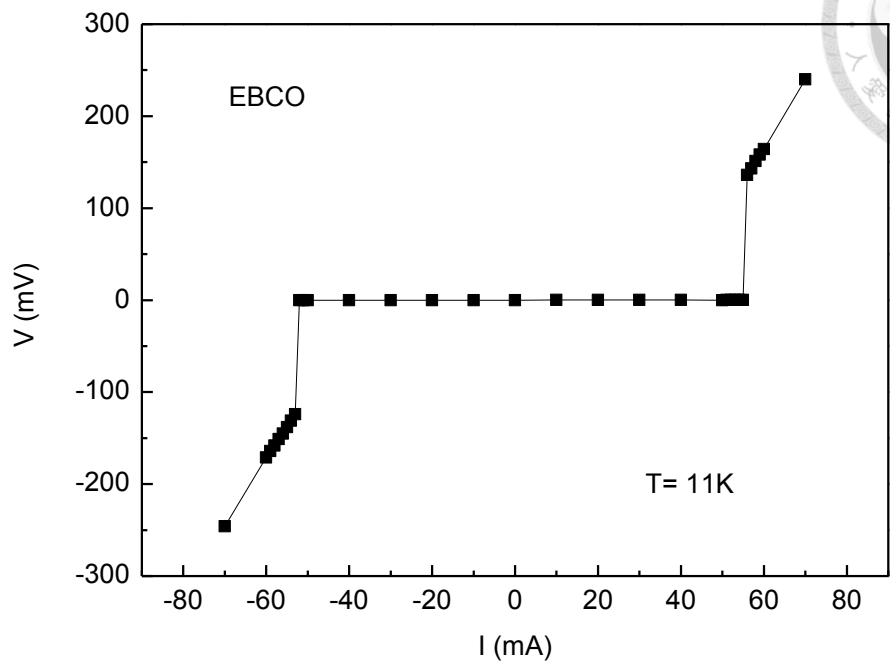


Figure 5.3.2: Shows the  $I$ - $V$  curve of the EBCO electrodes at  $T = 11$  K. The critical current can be seen at around  $I = 50$  mA.

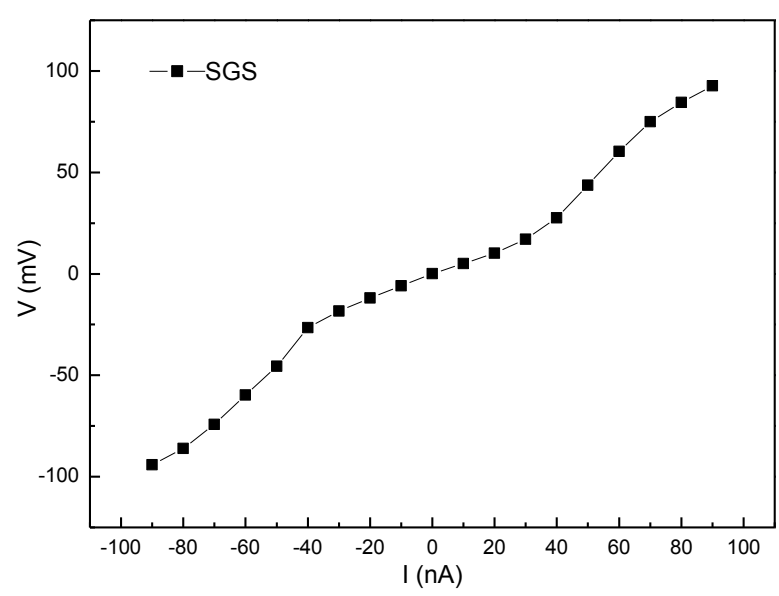


Figure 5.3.3: Shows the  $I$ - $V$  curve of the SGS junction at  $T = 11$  K.

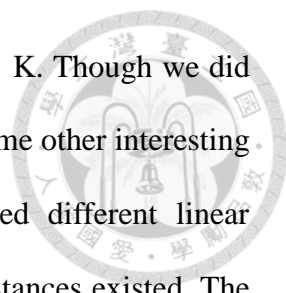


Figure 5.3.3 shows the  $I$ - $V$  curve of the SGS junction at  $T = 11$  K. Though we did not observe the conventional  $I$ - $V$  curve of Josephson junction [1], some other interesting physical properties can be extracted from the data. We observed different linear dependence in the  $I$ - $V$  curve of the SGS junction, i.e., different resistances existed. The resistance is lower when the injected current was between  $I = -40$  nA and  $I = 40$  nA. Once the current flow is outside of the aforementioned range, a higher resistance is observed. It means there exists a transition at a critical current value ( $I = \pm 40$  nA). It is suggested that the tunneling, which resulted in a lower resistance than that in a normal state, of the Cooper pairs is responsible for the transition. When the injected current exceeded a critical value, the coupling of the Cooper pairs was destroyed; giving rise to a higher resistance as shown in figure 5.3.2..

Although a perfect conventional  $I$ - $V$  curve was not observed on the SGS device in this study, the results of the investigation showed the existence of Josephson effect. The fact that a conventional  $I$ - $V$  curve for Josephson junction could be attributed to the contact resistance, which is too large, between graphene and EBCO. The quality of the graphene/EBCO interface is a crucial factor in the future investigation of the SGS systems.

## References



- [1] Peter Rickhaus, Markus Weiss, Laurent Marot, and Christian Schönenberger, *Nano Lett.* **12**, 1942–1945 (2012).
- [2] Dongchan Jeong, Jae-Hyun Choi, Gil-Ho Lee, Sanghyun Jo, Yong-Joo Doh, and Hu-Jong Lee, *Phys. Rev. B* **83**, 094503 (2011)

## Chapter 6 Conclusion



In this thesis, current heating effect was utilized to study the scattering mechanisms, electron-phonon and electron-electron scatterings, in a two-dimensional electron system, i.e., the epitaxial graphene. The same result from weak localization and phase coherent rate used as different thermometers to measure the electron effective temperature  $T_e$  suggested that electron-phonon scattering dominated in the epitaxial graphene. However, electron-electron scattering was also observed from the linear temperature dependence of phase coherence rate at the low temperature.

In general, it is difficult to study electron-electron and electron-phonon scatterings independently. The results of the analyses of the experiments data suggested that the electron heating effect is a powerful tool for studying two inelastic scattering properties and physical phenomena in the two-dimensional system or the nanostructures.

An interesting transition observed in the measured  $I$ - $V$  curve of the SGS junction suggested the existence of Josephson effect although the conventional  $I$ - $V$  curve of Josephson junction was absent possibly due to the quality of the graphene/EBCO interface. More effort on improving the interface quality would be beneficial to the further investigations of SGS systems in the future.